Boundary-Layer Meteorology manuscript No.
(will be inserted by the editor)

The Role of Large-Coherent-Eddy Transport in the Atmospheric Surface Layer Based on CASES-99 Observations

Jielun Sun · Donald H. Lenschow · Margaret A. LeMone · Larry Mahrt

Received: DD Month YEAR / Accepted: DD Month YEAR

Abstract The analysis of momentum and heat fluxes from the Cooperative Atmosphere-Surface Exchange Study 1999 (CASES-99) field experiment is extended throughout the diurnal cycle following the investigation of nighttime turbulence by Sun et al. (Journal of the Atmospheric Sciences, 2012, Vol. 69, 338-351). Based on the observations, limitations of Monin-Obukhov similarity theory (MOST) are examined in detail. The analysis suggests that strong turbulent mixing is dominated by relatively large coherent eddies that are not related to local vertical gradients as assumed in MOST. The HOckey-Stick Transition (HOST) hypothesis is developed to explain the generation of observed large coherent eddies over a finite depth and the contribution of these eddies to vertical variations of turbulence intensity and atmospheric stratification throughout the diurnal cycle. The HOST hypothesis emphasizes the connection between dominant turbulent eddies and turbulence generation scales, and the coupling between the turbulence kinetic energy and the turbulence potential energy within the turbulence generation layer in determining turbulence intensity. For turbulence generation directly influenced by the surface, the HOST hypothesis recognizes the role of the surface both in the vertical variation of momentum and heat fluxes and its boundary effect on the size of the dominant turbulence eddies.

Keywords Atmospheric boundary layer · Large coherent eddies · Momentum and heat fluxes · Non-local turbulent mixing

Jielun Sun
National Center for Atmospheric Research, P.O. Box 3000, Boulder, Colorado, 80307-3000, USA
Tel.: +1-303-497-8994
Fax: +1-303-497-8171
E-mail: jsun@ucar.edu

Donald H. Lenschow and Margaret A. LeMone
National Center for Atmospheric Research, P.O. Box 3000, Boulder, Colorado, 80307-3000, USA

Larry Mahrt
NorthWest Research Associates, Corvallis, Oregon, 97331-5503, USA

1 Introduction

For decades, Monin-Obukhov similarity theory (MOST) has been the cornerstone for turbulence parametrization in the surface layer of the atmospheric boundary layer (ABL), which we define as the bottom few decameters of the ABL. Departures from MOST have led researchers to divide the lower ABL into several layers (Fig. 1); in ascending order these are the roughness sublayer, the inertial sublayer where MOST is valid, and the outer layer where the effect of the surface on the airflow is negligible (e.g., Garratt, 1992). Nonetheless, because MOST is the only theory in use for turbulence parametrization in the surface layer, bulk formulae based on MOST are often used in situations where MOST may not be applicable.

The relationship between mean atmospheric variables and turbulence intensity, which is the goal of turbulence parametrization, has recently been examined for the nighttime boundary layer by Sun et al. (2012) (henceforth S12) using the month-long dataset collected from the Cooperative Atmosphere-Surface Exchange Study in October 1999 (CASES-99). They found that, when turbulence is generated by shear at night, turbulent mixing from the surface up to the highest turbulence observation height of 55 m can be categorized into three regimes depending on the relationship between turbulence variables and wind speed $\bar{V}(z)$ (the overbar represents a time average). The turbulence variable here can be any turbulent kinetic energy (TKE) related variable, such as the square root of TKE, $V_{TKE}(z) = [(1/2)(\sigma_u(z)^2 + \sigma_v(z)^2 + \sigma_w(z)^2)]^{1/2}$, or $\sigma_w(z)$ as used in S12, where $\sigma_u(z)$, $\sigma_v(z)$, and $\sigma_w(z)$ are the standard deviations of the zonal, meridional, and vertical wind components. There are two dominant regimes—a weak and a strong turbulence regime—separated by a threshold averaged wind speed, $\bar{V}_s(z)$, at a given height z; $V_{TKE}(z)$ increases linearly with $\bar{V}(z)$ in the strong turbulence regime, and is weakly correlated but still mostly increasing with $\bar{V}(z)$ in the weak turbulence regime. As the plot of the dramatic transition between the weak and strong turbulence regimes resembles a hockey stick, Sun et al. (2015) referred to this as the HOckey-Stick Transition (HOST). The observations in S12 clearly demonstrate that dominant turbulent eddies have a finite length scale δz and turbulence generation is related to shear, $\delta\bar{V}(z)/\delta z$, as opposed to a scale derived from the local derivative $\partial\bar{V}(z)/\partial z$. In the strong turbulence regime, the dominant turbulence eddies scale with z, indicating that they are generated by bulk shear $\bar{V}(z)/z$, i.e., $\delta z = z$. As the stability increases, the size of the dominant turbulence eddies gradually becomes less than z but finite, indicating that they are generated by $\delta\bar{V}(z)/\delta z$ rather than $\partial\bar{V}(z)/\partial z$ as assumed for all stability conditions in MOST. In other words, large eddies with a scale δz that predominantly contribute to turbulence intensity are not governed by $\partial\bar{V}(z)/\partial z$, especially under neutral conditions. In addition to the weak and strong turbulence regimes, occasionally relatively strong turbulence can be transported downward to height z even if $\bar{V}(z) < \bar{V}_s(z)$, which is the third regime in S12. Overall, the importance of S12 is its documentation of the contribution of coherent eddies of finite scales to turbulent mixing. Here coherent eddies refer to large eddies that efficiently transport momentum and heat.

The general concept of turbulent mixing across finite scales above the surface, also referred to as non-local mixing, has been previously discussed by, for example, Stull (1984), Högström et al. (2002), Zilitinkevich (1995), and Zilitinkevich et al. (2006). Large rolls in the convective ABL have also been observed to transport momentum and heat, as reviewed in Etling and Brown (1993). The new idea from the observations in S12 is that the scale of eddies responsible for turbulent mixing under near-neutral conditions is well-defined and related to the local wind speed in the surface layer. As the atmospheric stability increases, the scale of the dominant eddies decreases, but remains finite.

The relationship between strong winds and strong turbulence has been noted previously (e.g., King et al., 1994; Acevedo and Fitzjarrald, 2003). Since the publication of S12, HOST has been confirmed at various sites (e.g., van de Wiel et al., 2012; Mahrt et al., 2013, 2015; Martins et al., 2013; Bonin et al., 2015). van de Wiel et al. (2012) found that the net radiation is also a factor in determining $\bar{V}_s(z)$. By comparing observations from three field experiments, Mahrt et al. (2013) suggested that $\bar{V}_s(z)$ might decrease with increasing surface roughness. Recently, Mahrt et al. (2015) found that although HOST is characterized by the dramatic variation of turbulence intensity with $\bar{V}(z)$, the vertical potential temperature difference between the observation height and the surface also plays a role in $\bar{V}_s(z)$.

In this paper, after discussing the observations in Sect. 2, we examine MOST in detail in Sect. 3. We then further extend the nighttime analysis in S12 and include analyses of daytime turbulence generation, and the transport of momentum and heat (Sect. 4). In Sect. 5, we investigate vertical variations of daytime and nighttime momentum and heat fluxes in comparison with the MOST bulk formulae. Section 6 is a summary, where we generalize the explanation for the observed diurnal and vertical variation of momentum and heat fluxes as the HOST hypothesis.

2 Observations

The dataset used herein was obtained from 60-m tower measurements during CASES-99 (Poulos et al., 2002; Sun et al., 2002, 2013). Three-dimensional sonic anemometers were installed at heights of 10 m, 20 m, 30 m, 40 m, 50 m, and 55 m above the ground on the 60-m tower. Two additional sonic anemometers were installed at 1.5 m and 5 m above the ground on a 10-m tower, 10 m east of the 60-m tower to avoid flow distortion from the base of the 60-m tower. The observations referred to in this study as 60-m tower observations actually came from both towers. The lowest sonic anemometer was moved to the 0.5-m level from 1.5 m on 20 October. In addition to the eight sonic anemometers, the wind speed and direction were also measured by prop-vanes at heights of 15 m, 25 m, 35 m, and 45 m. Air temperature was measured by Väisälä temperature/humidity sensors at six levels (Sun et al., 2002) and by 34 thermocouples with a vertical spacing of 1.8 m from 2.3 m to 58.1 m height on the 60-m tower, and also at 0.23 m and 0.63 m on two adjacent posts, which were about 1 m from the 60-m tower. Net radiation, R_{net}, was measured by net radiometers at six satellite stations surrounding the 60-m tower, and was used to quantify the thermodynamic effect of the surface on turbulent mixing.

The sonic anemometer data were corrected for instrument axis misalignment using the method proposed by Wilczak et al. (2001) over the entire field experiment period (Sun, 2007). The difference between the corrected and uncorrected data is not significant.

Turbulent momentum fluxes are expressed as $u_*(z) = [\overline{w'u'}^2(z) + \overline{w'v'}^2(z)]^{1/4}$, where the prime of a variable represents a fluctuation from its time average. Similarly, the vertical potential temperature flux, which we refer to as the kinematic heat flux, $\overline{w'\theta'}(z)$, is expressed through the temperature scale, $\theta_*(z) \equiv -\overline{w'\theta'}(z)/u_*(z)$, where θ is the potential temperature. We use the sonic temperature for turbulence statistics involving virtual temperature since the difference between them has negligible impact on the statistics because of the relatively low humidity. Turbulence variables at the lowest measurement level, which is 1.5 m before 20 October and 0.5 m afterward, are used to represent turbulence at the surface, and are denoted by the subscript 0. For example, the Obukhov length is $L \equiv \bar{\theta}_0 u_{*0}^2/(\kappa g \theta_{*0})$, where g is the acceleration due to gravity, and κ is the von Kármán constant. The aerodynamic roughness length $z_m = 0.05$ m (defined in Sect. 3) is obtained using the high wind-speed data only (Sun, 2011). The near-surface $\bar{\theta}_0$ value is obtained from the lowest thermocouple measurement at 0.23 m.

Momentum and heat fluxes are calculated from Haar wavelet cospectra integrated over 30-min segments (Howell and Mahrt, 1994; Howell, 1995; Howell and Sun, 1999). To avoid "random" temporal influences of submeso disturbances on turbulent fluxes especially under stable conditions (Mahrt, 2009), the lowest frequency at which cospectra contributing to fluxes for each segment are well-behaved is determined for each segment by visual inspection. Because the averaged relationship between turbulent fluxes and mean variables using the 30-min dataset closely agrees with that using the 5-min dataset when turbulence variables are calculated using unweighted block averages from the 5-min segments, we focus on the 30-min flux data and use the 5-min flux data to increase the number of overall data points. Under near-neutral conditions, the turbulent momentum fluxes are almost entirely due to the along-wind turbulent momentum fluxes, $\overline{w'V'}_{along}(z) \approx \overline{w'V'}(z)$, where $V(z) = \sqrt{u^2(z) + v^2(z)}$ and $V_{along}(z)$ is the wind speed in the wind direction. In the 5-min dataset, 24% of the periods have $|L| > 100$ m, i.e., near-neutral; 29% have -100 m $< L < 0$, i.e., unstable; and 47% have $0 < L < 100$ m, i.e., stable.

All twelve levels of wind measurements at a given time are used to calculate the local shear $\partial\bar{V}(z)/\partial z$ as described in Sun (2011). In brief, the wind speeds at three measurement levels—one at height z, one below, and one above— are fitted with a log-linear function of z, and local shear is calculated using this locally-fitted wind profile. Although $|\partial\bar{\mathbf{V}}(z)/\partial z| \geq \partial\bar{V}(z)/\partial z$, where $\partial\bar{\mathbf{V}}(z)/\partial z$ and $\partial\bar{V}(z)/\partial z$ denote a vector and a speed shear, respectively, the two differ only when wind speed is low as the vertical variation of wind direction is almost eliminated by strong mixing associated with strong winds. We use $\partial V(z)/\partial z$ here to focus comparison between MOST and observations under strong mixing conditions as the weak wind regime is beyond the scope of this study because of the difficulty in estimating δz. Thus the local gradient Richardson number is $Ri(z) = (g/\bar{\theta}_0)[\partial\bar{\theta}(z)/\partial z]/[(\partial\bar{u}(z)/\partial z)^2 + (\partial\bar{v}(z)/\partial z)^2] \approx (g/\bar{\theta}_0)[\partial\bar{\theta}(z)/\partial z]/[\partial\bar{V}(z)/\partial z]^2$.

All times are UTC, which is 6 h ahead of local standard time. Daytime and nighttime are defined when R_{net} switches sign. The nighttime defined by zero downward solar radiation is slightly longer than the one defined by R_{net} at the site, which does not affect the conclusions.

3 MOST

Parametrizing vertical turbulent momentum transport based on vertical wind shear can be traced back to Boussinesq (1877), who assumed that the formulation for turbulent mixing is similar to that for molecular diffusion. Later, Prandtl (1925) introduced the concept of a mixing length $l(z)$, where $l(z) = u_*(z)/[\partial \bar{V}(z)/\partial z]$. Von Kármán (1930), who was Prandlt's student, found that near the surface, $l(z) = \kappa z$.

Obukhov (1946) and Monin and Obukhov (1954) recognized the influence of the stability on l, and introduced a stability function Φ such that $l(z, Ri) = l_n(z)\Phi(Ri)$, where the subscript n represents the neutral condition, and $l_n(z) \equiv \kappa z$. In addition, based on the assumed analogy between momentum and heat transfer, Monin and Obukhov extended their relation for momentum transfer to heat transfer (McNaughton, 2009). The well-known MOST equations were originally expressed as functions of Ri, i.e.,

$$\frac{\kappa z}{u_{*0}} \frac{\partial \bar{V}(z)}{\partial z} = \Phi_m(Ri), \tag{1}$$

$$\frac{\kappa z}{\theta_{*0}} \frac{\partial \bar{\theta}(z)}{\partial z} = \Phi_h(Ri), \tag{2}$$

where Φ_m and Φ_h are the stability functions for momentum and heat, respectively, and need to be determined from observations (e.g., Högström, 1996).

The non-dimensional ratio z/L is related to Ri using Eqs. 1 and 2 as

$$Ri(z) = (z/L)\ \Phi_h/\Phi_m^2. \tag{3}$$

As L represents a length scale associated with turbulence, the ratio z/L can be seen as a measure of the turbulence eddy scale relative to z. The atmosphere is considered neutral when $|z/L| \approx 0$, i.e., $|L| \to \infty$. In practice, the neutral ABL is commonly associated with $|L| > 100$ m. A small $|z/L|$ value could result from a very large $|L|$ or a near-zero z and a not-very-large L, suggesting that the atmospheric stability near the surface is always near-neutral, and not easily influenced by L variations. In contrast, for large z, z/L is more sensitive to L variations.

Using the concept of the mixing length, Eqs. 1 and 2 can be alternatively expressed as

$$l_m(z, z/L) \equiv u_{*0}/\frac{\partial \bar{V}(z)}{\partial z} = l_{mn}(z)/\Phi_m(z/L) = \kappa z/\Phi_m(z/L), \tag{4}$$

$$l_h(z, z/L) \equiv \theta_{*0}/\frac{\partial \bar{\theta}(z)}{\partial z} = l_{hn}(z)/\Phi_h(z/L) = \kappa z/\Phi_h(z/L), \tag{5}$$

where l_m and l_h are the mixing lengths for momentum and heat, respectively. Equations 4 and 5 clearly show that l_m and l_h at a given z under any stability condition are equal to their neutral values at z, $l_{mn}(z)$ and $l_{hn}(z)$, modified by their corresponding stability functions. Under the influence of the surface, the neutral mixing length is proportional to z, i.e., $l_{mn} = l_{hn} \equiv \kappa z$, which determines the vertical validity of MOST.

Assuming $u_*(z)$ and $\theta_*(z)$ are approximately constant with height near the surface, $u_*(z)$ and $\theta_*(z)$ within this layer, which are expressed as u_{*0} and θ_{*0}, respectively, can be formulated in terms of mean variables $\bar{V}(z)$ and $\bar{\theta}(z)$ by vertically integrating Eqs. 1 and 2. The vertically integrated formulae, i.e., the bulk relation, are then

$$\overline{w'V'}_0 \equiv u_{*0}^2 = C_d(z)\bar{V}(z)^2, \tag{6}$$
$$\overline{w'\theta'}_0 \equiv -u_{*0}\theta_{*0} = -C_h(z)\bar{V}(z)[\bar{\theta}(z) - \bar{\theta}_0] = -C_h(z)\bar{V}(z)\Delta\bar{\theta}(z), \tag{7}$$

which are widely used for parametrizing near-surface turbulence in numerical models. In Eqs. 6 and 7, C_d and C_h are the drag coefficient and the exchange coefficient for heat, respectively, and are expressed as

$$C_d(z) = \frac{\kappa^2}{[\ln(z/z_m) - \Psi_m(z/L)]^2}, \tag{8}$$
$$C_h(z) = \frac{\kappa^2}{[\ln(z/z_m) - \Psi_m(z/L)][\ln(z/z_h) - \Psi_h(z/L)]}, \tag{9}$$

where z_m and z_h are the aerodynamic roughness length and the roughness length for heat, and Ψ_m and Ψ_m are the vertically integrated Φ_m and Φ_h, respectively. Later in Sect. 5 we use the stability functions presented in Beljaars and Holtslag (1991). Note that the approximate constancy of $u_*(z)$ and $\theta_*(z)$ is not required for Eqs. 1 and 2 except in the surface layer for deriving the bulk formulae. Mathematically z_m and z_h are fitted parameters such that the observed momentum and heat fluxes satisfy Eqs. 6 and 7, respectively (Sun and Mahrt, 1995).

The validity of MOST clearly relies on the implicit assumptions of stationarity and horizontal homogeneity near the surface as well as the explicit assumptions listed above. Non-stationarity results in scatter in the relationships between the stability functions and the stability parameters Ri or z/L in MOST (e.g., Mahrt, 2007). By examining the vertical variation of l_{mn} and l_{hn} using the CASES-99 dataset, Sun (2011) found that the layer where MOST is valid is approximately between 0.5 m and 10 m during CASES-99. This depth increases with wind speed (Peña et al., 2010), i.e., if wind speed were greater than that observed during CASES-99, the upper height for the validity of MOST would be > 10 m. Commonly, MOST is assumed approximately valid in the bottom 10% of the ABL layer but above the roughness sublayer (Sect. 1), which is substantially different from the observed depth for MOST during CASES-99 (more in Sect. 5).

Another important issue regarding MOST is self-correlation that occurs in determining Φ_m and Φ_h. Although the issue has been studied, for example, by Hicks (1978), Andreas and Hicks (2002), Klipp and Mahrt (2004), Baas et al. (2006), and Mahrt (2007, 2008), a clear example is provided here using the CASES-99 dataset because self-correlation is still often ignored in the research community. Due to the common factor $\partial\bar{\theta}(z)/\partial z$ in both Φ_h and Ri, the well-known relationship between Φ_h and Ri can be reproduced by even randomly generated $\partial\bar{\theta}(z)/\partial z$ (Fig. 2a), which clearly illustrates that Φ_h is strongly influenced by its self-correlation with Ri. However, self-correlation may not always artificially enhance the actual physical relationship between turbulence intensity and mean variables as in the relationship between Φ_h and Ri; it can sometimes undermine it as in the relationship between Φ_m and Ri (Fig. 2b). Thus, it is important to examine non-dimensional relationships by, for example, replacing common parameters in both the abscissa and ordinate with randomly generated numbers as in Fig. 2.

4 Observed relationships between mean and turbulent variables

Here we investigate how daytime and nighttime momentum and heat fluxes vary with height over the relatively deep tower layer during CASES-99. Both atmospheric stratification and shear affect turbulence intensity, and the two factors are related. To clarify the concept, which is essential for explaining the observed turbulent mixing using mean variables, we first describe the evolution of the vertical temperature gradient and its relationship with turbulent mixing in the ABL even though it may seem to be elementary. To simplify the discussion here, we ignore heating and cooling in the ABL due to, e.g., aerosols and clouds (Sun et al., 2003).

Because surface heating and cooling are the main heat source and sink for the diurnal variation of the ABL, vertical variations of temperature in the ABL mainly result from the vertical redistribution of warm/cold air from the surface by turbulent mixing. Therefore, temperature profiles in the tower layer mainly depend on the generation of warm or cold air through molecular thermal conduction or diffusion in a relatively thin layer adjacent to the surface and turbulent transfer above the molecular diffusion layer. Longwave radiative cooling at the surface provides the cold air source to the ABL at night (e.g., Sun et al., 1995, 2003); solar radiative heating at the surface provides the warm air source to the ABL during daytime. The air cooled by molecular diffusion adjacent to the surface is mixed upward by shear-driven turbulence and replaced by warmer air from above. The air warmed by molecular diffusion adjacent to the surface spontaneously generates convection since it is lighter than the overlying air. The evolving balance between turbulent mixing from above and molecular diffusion from below leads to a range of air-surface temperature differences.

Turbulence can be generated by either shear or positive buoyancy at the surface, but the two processes affect the vertical temperature gradient differently. Shear-generated turbulent mixing is a mechanical mixing, which leads to a more uniform temperature in the mixing domain. This mixing can increase the vertical temperature gradient above the thin molecular diffusion layer once the mixing starts to transport the cold air accumulated in the thin layer near the surface upward. If the mixing increases and persists, it can reduce the vertical temperature gradient once the cold air supply from molecular diffusion becomes less than the vertical distribution of the cold air by the mixing. In contrast, surface positive buoyancy generates turbulence thermally through temperature decreasing with height.

The vertical gradient of potential temperature can vanish throughout the diurnal cycle if shear-generated turbulence dominates the mixing in the daytime and is sufficiently strong at night. Thus, the nighttime ABL is not necessarily stably stratified, and the daytime ABL is not necessarily unstably stratified. Because the maximum $|R_{net}|$ is much smaller at night than during daytime, near-neutral conditions near the surface can more often form at night than during daytime for a given high wind speed. The month-long observations during CASES-99 indicate that the vertical $\overline{\theta}(z)$ gradient near the surface can be reduced to nearly zero at night but not readily during daytime unless R_{net} is small or wind speed is very high (Fig. 3). The correlation between turbulent mixing and the vertical temperature gradient is important in understanding vertical variations of momentum and heat fluxes in the ABL.

4.1 Nighttime momentum and heat fluxes

The nighttime relationship between $V_{TKE}(z)$ (defined in Sect. 1) and wind speed $\bar{V}(z)$ has been investigated by S12. Because $u_*(z)$ is well correlated with $V_{TKE}(z)$, the nighttime $u_*(z)$ in Figs. 4a and 4b has HOST behaviour similar to $V_{TKE}(z)$. Here we focus on the effect of the bulk potential temperature difference $\Delta\bar{\theta}(z)$

$$\Delta\bar{\theta}(z) = \int_{z=0.23m}^{z} \frac{\partial\bar{\theta}(z)}{\partial z} dz = \bar{\theta}(z) - \bar{\theta}_0, \tag{10}$$

on $u_*(z)$ in the HOST, which was not discussed in detail in S12. When $\bar{V}(z) > \bar{V}_s(z)$ (defined in Sect. 1), large $u_*(z)$ is generated by $\bar{V}(z)/z$, and large eddies with scale z lead to a well-mixed turbulent layer with a small $\Delta\bar{\theta}(z)$ (e.g., the wind and potential temperature profiles shown in red in Figs. 4c and 4d). In other words, the atmosphere near the surface can reach near-neutral conditions just as if R_{net} were near zero (more in Sect. 5). When $\bar{V}(z) < \bar{V}_s(z)$, small $u_*(z)$ at height z leads to a shallow mixing layer with its depth determined by the vertical length scale of the shear, $\delta z < z$ as documented by S12 (e.g., the wind and potential temperature profiles shown in green in Figs. 4c and 4d). That is, turbulent eddies at height z do not reach the surface. In this situation, cold air near the surface cannot directly reach height z, resulting in a large $\Delta\bar{\theta}(z)$. A large fraction of nighttime turbulent mixing is weak (Fig. 5a).

Because of the dependence of $\Delta\bar{\theta}(z)$ on turbulent mixing, the relationship between $u_*(z)$ and $\Delta\bar{\theta}(z)$ depends on the turbulence regime. When $\bar{V}(z) < \bar{V}_s(z)$, $u_*(z)$ varies between zero and $u_{*s}(z)$, where $u_{*s}(z)$ is $u_*(z)$ at $\bar{V}(z) = \bar{V}_s(z)$ (Figs. 4a and 4b). When $\bar{V}(z) > \bar{V}_s(z)$, $\Delta\bar{\theta}(z)$ is reduced by turbulent mixing, and $u_*(z)$ does not vary much with $\Delta\bar{\theta}(z)$. Because $\Delta\bar{\theta}(z)$ represents a vertically integrated potential temperature difference, $|\Delta\bar{\theta}(z)|$ generally increases with z even when $|\partial\bar{\theta}(z)/\partial z|$ is small, which is reflected in the observed $\Delta\bar{\theta}(z) < 2$ K at 10 m and < 1 K at 5 m in Figs. 4a and 4b, respectively. Naturally the relationship between $u_*(z)$ and $\Delta\bar{\theta}(z)$ also depends on the history or non-stationarity of turbulent mixing because $\Delta\bar{\theta}(z)$ reflects the consequence of turbulent heat transfer and the build-up of the cold air near the surface over a period of time.

Because $\theta_*(z)$ is traditionally studied as a function of the vertical potential temperature gradient, $\partial\bar{\theta}/\partial z$, here we compare the dependence of $\theta_*(z)$ on $\Delta\bar{\theta}(z)$ and $\bar{V}(z)$ at 5 m (Fig. 6); similar results can be found at the other levels (Fig. 7). Under nighttime stable conditions, the observed $\theta_*(z)$ is better correlated with $\bar{V}(z)$ than with $\Delta\bar{\theta}(z)$ (Fig. 6) and $\partial\bar{\theta}/\partial z$ (not shown). This indicates that under stable conditions turbulent mixing affects temperature variances more than thermal stratification does.

When $\bar{V}(z) < \bar{V}_s(z)$ and $\Delta\bar{\theta}(z)$ is relatively large, $\theta_*(z)$ is limited by vertical velocity fluctuations, which are directly related to $\bar{V}(z)$ (Fig. 6a), resulting in $\theta_*(z)$ being mainly dependent on $\bar{V}(z)$ instead of $\Delta\bar{\theta}(z)$ (inset in Fig. 6b). For small z, $\theta_*(z)$ approximately linearly increases with $\bar{V}(z)$ when $\bar{V}(z) < \bar{V}_s(z)$ (Fig. 7a); for large z, $\theta_*(z)$ remains near-zero when $\bar{V}(z) \ll \bar{V}_s(z)$ as turbulent eddies at height z do not reach the surface, and increases sharply with $\bar{V}(z)$ when $\bar{V}(z) \to \bar{V}_s(z)$.

When $\bar{V}(z) > \bar{V}_s(z)$, strong turbulent mixing leads to the rapid reduction of the vertical potential temperature gradient (Figs. 4a and 4b), leading to the sharp decrease of $\theta_*(z)$ with $\bar{V}(z)$ (Figs. 6a and 7a). As demonstrated in S12, $\theta_*(z)$

reaches its maximum value, $\theta_*^{max}(z)$, at $\bar{V}_s(z)$. Similar close relationships between $u_*(z)$ and scalar fluxes of, e.g., ozone, carbon dioxide, and water vapour have been observed by, for example, Sun and Massman (1999).

On a given night, $\theta_*^{max}(z)$ is influenced by the vertical temperature difference between the residual layer affected by the proceeding daytime heating and the near-surface layer resulting from the surface radiative cooling and molecular diffusion in transferring heat across the air-land interface. When the afternoon heating is reduced by clouds and the wind speed is high at night, $\Delta\bar{\theta}(z)$ is relatively small, leading to a relatively small $\theta_*^{max}(z)$. During CASES-99, the maximum downward solar radiative flux was mostly around 700 W m^{-2} except for 16 October when it reached about 400 W m^{-2}. In addition, $\bar{V}(z)$ was relatively large for this night. As a result, the decrease of $\theta_*(z)$ with $\bar{V}(z)/\bar{V}_s(z)$ from this night is shifted below the $\theta_*(z)$-$\bar{V}(z)/\bar{V}_s(z)$ relationship for the other nights (red dots in Fig. 6 are primarily from the night of 16 October). The relationship between $\theta_*(z)$ and $\Delta\bar{\theta}(z)$ when the positive nighttime $\Delta\bar{\theta}(z)$ approaches zero, i.e., the neutral condition, is consistent with its relationship when the negative daytime $\Delta\bar{\theta}(z)$ approaches zero (more in in Sect. 4.3).

Because $\theta_*(z)$ and $u_*(z)$ have opposite dependency on $\bar{V}(z)$ when $\bar{V}(z) > \bar{V}_s(z)$ and a similar dependency on $\bar{V}(z)$ when $\bar{V}(z) < \bar{V}_s(z)$ (Figs. 4a, 4b, and 7a), the nighttime $|\overline{w'\theta'}(z)|$ increases with $\bar{V}(z)$ until it reaches a maximum value. The nighttime maximum downward $\overline{w'\theta'}(z)$ does not occur at $\bar{V}_s(z)$ as $\theta_*^{max}(z)$ does, but at $\bar{V}_{maxH}(z) > \bar{V}_s(z)$ (Fig. 7b). Because the rate of the $\theta_*(z)$ decrease with $\bar{V}(z)$ increases with z for $\bar{V}(z) > \bar{V}_s(z)$ (Fig. 7a), $\bar{V}_{maxH}(z)$ approaches $\bar{V}_s(z)$ as z increases (Figs. 5a and 7a). This maximum downward heat flux at night has also been observed by, for example, Mahrt et al. (1998), and van de Wiel et al. (2007, 2012); our observations indicate that its occurrence is not only a function of stability, but also of height z.

4.2 Threshold wind speed

The role of stable stratification in turbulent mixing has been extensively investigated, and $\partial\bar{\theta}(z)/\partial z$ is commonly believed to be the key variable in determining turbulence intensity as evidenced in numerical and laboratory experiments (e.g., Hopfinger, 1987; Lindborg, 2006). Because buoyancy fluxes are associated with both TKE and turbulent potential energy (TPE, which is also called available potential energy by Holliday and McIntyre (1981)), where $TKE = (1/2)(\overline{V'^2} + \overline{w'^2})$, $TPE = (1/2)[g/(T_0N)]^2\overline{(\theta')^2}$ (Zilitinkevich et al., 2007), N is the Brunt-Väisälä frequency, and T_0 is a reference air temperature, shear-generated turbulence in a stably stratified flow can result in variations of both TKE and TPE through buoyancy fluxes (Ostrovsky and Troitskaya, 1987). According to Zilitinkevich et al. (2007), the total turbulence energy ($TTE = TKE + TPE$) can be achieved by combining the TKE and TPE equations through cancellation of buoyancy fluxes in both equations, resulting in,

$$\frac{D\ TTE}{Dt} + \frac{\partial \Phi_T}{\partial z} = -\overline{w'V'}\frac{\partial \bar{V}(z)}{\partial z}, \tag{11}$$

where Φ_T is the vertical flux of TTE, i.e., $\Phi_T = \Phi_K + [g/(T_0N)^2]\Phi_\theta$, $\Phi_K \equiv (1/\bar{\rho})\ \overline{p'w'} + (1/2)\ \overline{V'^2w'}$ (ρ is the air density, and p is the air pressure) and

$\Phi_\theta = (1/2)\ \overline{(\theta')^2 w'}$. Note that all the terms in Φ_T are third-moment except $\overline{p'w'}$. Equation 11 indicates that if $\partial \Phi_T/\partial z$ is relatively small, the turbulence shear production on the right side of Eq. 11 controls the variation of TTE. For a flow with a given turbulence shear production and negligible $\partial \Phi_T/\partial z$ (e.g., Lenschow et al., 1988), TKE of the flow would be reduced if imposed stable stratification on the flow increases because more turbulence energy is used to increase TPE as shown in both laboratory and numerical simulations (e.g., Lin and Pao, 1979). If the stable stratification is reduced, TKE would increase with a given shear. That is, TKE and TPE are dynamically coupled, thus momentum and heat fluxes are connected. Stable stratification does not eliminate TKE but converts TKE to TPE as shown in Eq. 11.

The nighttime observed dependence of $u_*(z)$ and $\theta_*(z)$ on $\bar{V}(z)$ and $\Delta\bar{\theta}(z)$ confirms the close connection between TKE and TPE through turbulent mixing generated by shear. When $\bar{V}(z)$ is small, the vertical redistribution rate of cold air through weak turbulent mixing is mainly near the surface while the air temperature at greater heights is not affected. As a result, $\Delta\bar{\theta}(z)$ can increase if $\bar{\theta}_0$ in Eq. 10 decreases (Fig. 4d). Once the turbulence mixing is sufficiently strong, the large coherent eddies dominating transport grow to scale with z, and the vertical potential temperature gradient below z is significantly reduced by turbulent mixing because the cold-air generation process is slow compared to the turbulent heat transport. Therefore the observed HOST in S12 (Fig. 4) essentially indicates that when $\bar{V}(z) < \bar{V}_s(z)$, the increase of TKE near the surface is constrained by the energy used for increasing TPE through the buoyancy flux; thus TKE does not increase significantly with increasing $\bar{V}(z)$. When $\bar{V}(z) > \bar{V}_s(z)$, the vertical potential temperature gradient below z is effectively eliminated by large turbulent eddies with scale z, and shear generates TKE directly without being consumed to increase TPE. This changing TPE consumption mechanism as $\bar{V}(z)$ exceeds $\bar{V}_s(z)$ leads to a dramatic increase of TKE with $\bar{V}(z)$. Therefore, $\bar{V}_s(z)$ represents a statistically-averaged $\bar{V}(z)$ associated with the critical shear at z; when $\bar{V}(z) > \bar{V}_s(z)$, the vertical potential temperature gradient in the layer between the surface and z can be virtually eliminated. In other words, even though $\overline{\theta'}^2$, $\theta_*(z)$, and $\overline{w'\theta'}$ may not be zero for $\bar{V}(z) > \bar{V}_s(z)$, the turbulence energy used for increasing TPE is considerably reduced, leading to a significant increase with $\bar{V}(z)$ in variables related to TKE, such as $V_{TKE}(z)$, $\sigma_w(z)$, and $u_*(z)$.

The strong dependence of any TKE-related variable on $\bar{V}(z)$ and weak dependence on the vertical potential temperature gradient in HOST is simply due to the fact that coherent eddies with finite scales contribute significantly to turbulence mixing, and turbulent mixing shapes the vertical potential temperature gradient. In other words, because the vertical potential temperature gradient and turbulence intensity are dynamically coupled, the wind-speed variation in the HOST of any TKE-related variable naturally separates the stable regime for $\bar{V}(z) < \bar{V}_s(z)$ and the near-neutral regime for $\bar{V}(z) > \bar{V}_s(z)$.

As the energy required for eliminating the vertical potential temperature gradient in the layer between the surface and height z increases with the depth of the layer, $\bar{V}_s(z)$ increases with z. To capture the variation of turbulence intensity dominated by large coherent eddies on the scale of z, factors affecting the TTE balance within the layer between the surface and height z, including turbulence shear-generation within the layer and boundary conditions, need to be considered. Therefore, the HOST of any TKE-related variable can be affected by surface roughness and effective surface heating/cooling (more in Sect. 5). The surface effect on HOST has been observed by van de Wiel et al. (2012), Mahrt et al. (2013), and Mahrt et al. (2015).

S12 demonstrated that the mixing length based on the local momentum and heat fluxes increases dramatically when $\bar{V}(z)$ undergoes transition from $\bar{V}(z) < \bar{V}_s(z)$ to $\bar{V}(z) > \bar{V}_s(z)$, suggesting that the increase of $u_*(z)$ dominates the increase of L because $u_*(z)$ increases linearly with $\bar{V}(z)$ and $\theta_*(z)$ decreases with $\bar{V}(z)$; $\bar{V}_s(z)$ essentially separates the near-neutral from the stably-stratified nighttime surface layer. Even though technically the neutral atmosphere corresponds to $|L| \to \infty$, which can only be approximated in the atmosphere under strong winds, characteristics of turbulent mixing in the strong turbulence regime are similar to the neutral atmosphere. The small vertical potential temperature gradient for $\bar{V}(z) > \bar{V}_s(z)$ changes only slightly with increasing $\bar{V}(z)$.

4.3 Daytime momentum and heat fluxes

During daytime, turbulence generation is dominated by positive buoyancy from the heated surface with an additional contribution from shear as observed by, for example, Williams and Hacker (1992). Large coherent eddies generated by positive buoyancy from the heated surface contribute to the heat flux as well as to the momentum flux, which enhances $u_*(z)$ compared to the nighttime HOST (Fig. 8) except at $z = 0.5$ m (more in Sect. 4.5). Because of the vertical momentum transfer over a relatively deep layer by large coherent eddies generated by positive buoyancy fluxes, $\bar{V}(z)$ is enhanced near the surface and reduced above, which explains the significantly greater fraction of $\bar{V}(z) > \bar{V}_s(z)$ points for $z < 20$ m than for $z > 20$ m (Fig. 5b). Here we only use $\bar{V}_s(z)$ as a reference for a relatively high $\bar{V}(z)$ at each z because $\bar{V}_s(z)$ determines the transition between the stably-stratified and near-neutral nighttime turbulence regimes as described in Sect. 4.2. Because buoyancy flux is related to R_{net}, the enhancement of $u_*(z)$ by buoyancy flux can be clearly viewed in the increase of $u_*(z)$ with $\bar{V}(z)$ as a function of R_{net} (Fig. 9). Furthermore, Fig. 9 indicates that the buoyancy enhancement of $u_*(z)$ is significant except at $z = 0.5$ m (more in Sect. 4.5) or when $\bar{V}(z)$ is large. The influence of R_{net} on $u_*(z)$ becomes more significant with increasing z especially when the wind speed is low. For example, the greatest increase of $u_*(z)$ with R_{net} is for $\bar{V}(z) < 2$ m s^{-1} at 55 m. Also, the change of $u_*(z)$ with R_{net} decreases with increasing R_{net} for a given wind-speed range.

In contrast to the nighttime $\theta_*(z)$, daytime $\theta_*(z)$ is strongly correlated with $\Delta\bar{\theta}(z)$, but not so much with $\bar{V}(z)$ (not shown) when positive surface buoyancy is the driving force for turbulent mixing. The observed $\theta_*(z)$–$\Delta\bar{\theta}(z)$ relationship remains unchanged above ≈ 20 m, suggesting that both $\bar{\theta}(z)$ and $\theta_*(z)$ become approximately invariant with z above ≈ 20 m as shown in Fig. 7d for -0.5 K $< \Delta\bar{\theta}(z) < 0$. The layer of constant $\theta_*(z)$ and $\bar{\theta}(z)$ above ≈ 20 m resembles the atmospheric mixed layer, which is often considered to be above the bottom 10% of the ABL, i.e., above about 100 m. Near the surface, both $\theta_*(z)$ and $\Delta\bar{\theta}(z)$ decrease sharply with z. Because $\theta_*(z)$ is actively maintained by positive buoyancy fluxes during daytime, the daytime $\theta_*(z)$ is non-zero even when $\bar{\theta}(z)$ is uniform for $z \geq 20$ m as the large coherent eddies at z are generated by buoyancy over a layer that scales with z (Sect. 4.4). The small fraction of the observed $|\theta_*(z)|$ that occurs at large $|\Delta\bar{\theta}(z)|$ and does not vary with $\Delta\bar{\theta}(z)$ is due to increasing correlation between w and θ at large $\Delta\bar{\theta}(z)$ (not shown). The observed daytime $\theta_*(z)$–$\Delta\bar{\theta}(z)$ relationship remains unchanged even when $\Delta\bar{\theta}(z)$ is slightly positive and wind speed is high at night, i.e., $\Delta\bar{\theta}(z) > 0$ and $\bar{V}(z) > \bar{V}_s(z)$ (Figs. 6b and 7c). Thus large coherent eddies generated by either convection or bulk shear contribute to the same $\theta_*(z)$–$\Delta\bar{\theta}(z)$ relationship valid for both unstable and near-neutral conditions.

4.4 Scale variations of turbulent eddies

The structure of large coherent eddies can be investigated through w spectra as in S12, and through vertical coherences of wind and temperature between different observational levels. We select three time periods to represent unstable, neutral, and stable surface layers for both analyses (Figs. 10 and 11). As in S12, for $\bar{V}(z) > \bar{V}_s(z)$, the normalized w spectra, $2\pi f S_w(z)/\sigma_w^2(z)$, where f is the frequency, $S_w(z)$ is the power spectrum of w, and $\sigma_w(z)$ is the standard deviation of w, from different heights all reach their peak values at the same normalized frequency $2\pi fz/\bar{V}(z) = 2$ (Fig. 10b). This result implies that if horizontal scales of turbulence eddies are represented by their half wavelengths, the horizontal scale of the dominant turbulent eddies equals z in response to the bulk shear $\bar{V}(z)/z$ under the near-neutral condition. Under stable conditions when $\bar{V}(z) < \bar{V}_s(z)$, the normalized w spectral peaks shift toward higher normalized frequency compared to their neutral values (Fig. 10c), indicating that the scale of dominant turbulent eddies decreases with increasing atmospheric stratification. Under convective conditions, the spectral peak for turbulent eddies generated by buoyancy flux shifts to a frequency less than 2 (Fig. 10a), suggesting that the horizontal size of dominant convective eddies is slightly larger than that under the near-neutral condition.

The vertical coherences of w, V, and θ between 55 m and all the underlying heights of the sonic anemometers as functions of wavenumber $k = 2\pi f/\bar{V}(z)$ for the same three stability cases as shown in Fig. 11 provide further evidence for large coherent eddies. Here the wavenumber k is calculated using $\bar{V}(z)$ at each of the underlying heights, which approximates the upper limit of k if $\bar{V}(z)$ increases with height. The differences in $\bar{V}(z)$ for the three stability cases account for the varying wavenumber cut-off. Under the near-neutral stability when turbulence is generated by strong shear (the middle column in Fig. 11), the relatively large decrease of the w coherence with increasing distance between 55 m and the underlying heights compared with the V coherence indicates that w varies significantly in the vertical compared with V. The near-constant large vertical coherence of θ at all heights reflects the similar temporal variation of θ at all heights in the near-neutral condition under strong winds.

Under the unstable condition, the vertical coherences of w and V are even larger than their neutral values at the small $k = 0.03$ m^{-1} for the underlying level $z \geq 5$ m, while the vertical coherence of θ is smaller than its neutral value (the left column in Fig. 11). These results suggest that the vertical variation of the horizontal size of convective eddies is smaller under the convective condition than the near-neutral condition for $z \geq 5$ m especially in the well-mixed layer above 20 m. The organized structure of large coherent convective eddies explains the observed increase of $u_*(z)$ and $\theta_*(z)$ with increasing $\Delta\bar{\theta}(z)$ in Sect. 4.3.

As the stable stratification increases when $\bar{V}(z) < \bar{V}_s(z)$ at night (the right column in Fig. 11), the vertical coherences of w and V for large eddies become smaller than their neutral values even between 55 m and 30-40 m at the smallest resolved $k \approx 10^{-2}$ m^{-1}, indicating the absence of large coherent eddies under stable conditions. The relatively large coherence of θ at small k and its sharp decrease with increasing k suggest that θ varies significantly between heights on relatively small scales due to the influence of small-scale turbulent mixing on θ under the stable condition, and that the decreasing trend of θ beginning in the evening and extending for the relatively long time scale of nearly 4 h is similar between 55 m and the underlying heights.

4.5 The near-neutral sublayer

The thinner the layer between the surface and height z, the smaller $\bar{V}(z)$ that is needed to mix the layer to a nearly uniform potential temperature. Therefore, $\bar{V}(z)$ adjacent to the surface can easily exceed $\bar{V}_s(z)$ from downward momentum transfer. We find that $|\Delta\bar{\theta}(z)|$ at $z = 0.5$ m is mostly < 1 K even when the surface is strongly heated, implying that the layer near the surface can be maintained at near-neutral stratification as a result of turbulent mixing regardless of the turbulence generation mechanism. As a result, $u_*(z)$ at $z = 0.5$ m increases approximately linearly with $\bar{V}(z)$ throughout the diurnal cycle (Fig. 8). This result suggests that the sublayer of $z < O(1)$ m is on average near-neutral all the time. Although the same conclusion may seem to be reached with MOST as $|z/L| \to 0$ when $z \to 0$, the MOST bulk formula does not perform well at 0.5 m especially under strong winds because the stability functions in the literature are based on observations above 0.5 m, where the atmospheric stability has greater variation (Sect. 5.3).

4.6 Richardson number

Since both positive buoyancy and shear generate turbulence, the combination of the two may seem to capture both contributions to turbulence generation. However, the length scale over which the Richardson number should be calculated is always an issue. Although $u_*(z)$ is clearly related to both $\bar{V}(z)$ and $\Delta\bar{\theta}(z)$ throughout the diurnal cycle, $u_*(z)$ is not well correlated with either the bulk Richardson number, $Ri_B(z) = (gz/\bar{\theta}_0)\Delta\bar{\theta}(z)/\bar{V}^2(z)$, or Ri for the entire range of stabilities (Fig. 12). From the above analyses, the size of the dominant turbulent eddies near the surface is, in general, δz, which is $\approx z$ under neutral and unstable conditions, and is $< z$ under stable conditions except very near the surface (Sect. 4.5). Under stable conditions, the shear for generation of these turbulent eddies is $\delta\bar{V}(z)/\delta z$, which approaches $\partial\bar{V}(z)/\partial z$ only when $\delta z \to 0$. Because $\bar{V}(z)/z$ is only responsible for the near-neutral turbulent mixing while its corresponding $\Delta\bar{\theta}(z)$ is strongly controlled by the strong turbulent mixing such as at night, Ri_B can only capture the variation of $u_*(z)$ under near-neutral conditions such as the windy cases as well as near the surface (Fig. 12). The small Ri values under strong mixing conditions reflect only the small $\partial\bar{\theta}(z)/\partial z$ resulting from strong mixing while $\partial\bar{V}(z)/\partial z$ can sometimes be invariant with z (e.g., Banta et al., 2003; Banta, 2008). In a stably stratified flow, because δz can be any value between zero and z, and turbulent eddies at z do not reach the surface, neither Ri_B nor Ri captures the variation of $u_*(z)$ for the entire range of observed stabilities (Fig. 12). Similar conclusions on the performance of Ri were reached by Caulfield and Kerswell (2001). The above analysis suggests that a robust relationship between turbulence intensity and any stability parameter for a range of stability conditions requires the stability parameter to capture the turbulence generation mechanism over the stability range, i.e., it has to be calculated on the scale of turbulence generation.

5 Vertical variation of the relationships between turbulence and mean variables in comparison with MOST

Based on the CASES-99 observations, we further explore how external factors such as surface roughness, surface heating/cooling reflected in R_{net}, and horizontal pressure gradients reflected in $\bar{V}(z)$, affect the observed relationships between $u_*(z)$, $\theta_*(z)$, $\bar{V}(z)$, and $\Delta\bar{\theta}(z)$ throughout the diurnal cycle. Here we ignore the small fraction of top-down turbulent mixing cases presented in S12, and focus on turbulent mixing generated near the surface. We investigate how $u_*(z)$ and $\theta_*(z)$ vary through simplified expressions based on the observations described in Sect. 4. We emphasize that these simple expressions only provide a basis for our investigation, and should not be used as new bulk formulae for parametrizing turbulence until more observational studies over different surfaces and weather conditions are made.

5.1 Vertical variation of $u_*(z)$

When turbulence is generated by strong shear, i.e., $\bar{V}(z) > \bar{V}_s(z)$, $u_*(z)$ can be approximately expressed as

$$u_*(z) = \alpha(z)\bar{V}(z) + \beta(z), \tag{12}$$

which is schematically shown in Fig. 13a. Under unstable conditions when the thermally-generated turbulence enhances $u_*(z)$ from its near-neutral $u_*(z) - \bar{V}(z)$ relationship, the enhancement mainly occurs under weak winds, thus Eq. 12 is approximately valid for daytime mixing as well. The influence of the surface mechanical effect on $u_*(z)$ can be isolated from the surface thermal effect under neutral conditions when strong turbulent mixing eliminates the atmospheric stratification or when $R_{net} \approx 0$.

To avoid complications associated with various empirically developed stability functions for the MOST bulk formulae in the literature, we first focus on comparing the observed $u_*(z)$ expressed in Eq. 12 with the formulated $u_*(z)$ based on MOST in Eq. 6 under the neutral condition. The observed $\alpha(z)$ near the surface under the neutral condition, i.e., when $\bar{V}(z)$ is large, is $\alpha_n(z) \approx u_*(z)/\bar{V}(z)$. The equivalent term in the MOST bulk formula for $u_*(z)$ under neutral conditions is

$$\alpha_n^{MOST}(z) = \frac{\kappa}{\ln(z/z_m)}, \tag{13}$$

and the equivalent $\beta(z)$ in MOST is

$$\beta_n^{MOST} = 0. \tag{14}$$

Using observations from the 60-m tower, we find that $\alpha(z)$ under neutral condition (i.e., $R_{net} \approx 0$), $\alpha_n(z)$, decreases sharply with height below 5-10 m, and remains nearly constant with height above (Fig. 13b). The decrease of $\alpha_n(z)$ with height near the surface indicates the reduced direct influence of the surface on turbulent momentum transfer with possible small influence of the atmospheric stratification because $\Delta\bar{\theta}(z)$ under strong wind conditions is only significant at large heights. Comparison between the observed $\alpha_n(z)$ and $\alpha_n^{MOST}(z)$ indicates that the two approximately agree below 10 m, and $\alpha_n^{MOST}(z)$ is consistently smaller than $\alpha_n(z)$ above 10 m. Changing z_m only shifts agreement between $\alpha_n^{MOST}(z)$ and $\alpha_n(z)$ from one level to another (more in Sect. 5.3). The difference between the observed $\alpha_n(z)$ and $\alpha_n^{MOST}(z)$ could also be related to the non-constant $u_*(z)$ with height even near the surface, which is observed by Sun et al. (2013).

Unlike $\alpha_n(z)$, the observed $\beta_n(z)$ decreases monotonically with z from its zero value at the surface, while β_n^{MOST} is zero regardless of z (Fig. 13c). The observed negative $\beta_n(z)$ reflects the required increasing shear for the increasing depth of the air layer to generate strong turbulent mixing for reducing the atmospheric stratification to near zero. The observed non-zero $\beta_n(z)$ further suggests that turbulent mixing within the layer between the surface and height z needs to be considered for determining turbulent intensity at z, which is excluded in the MOST bulk formula (more in Sect. 5.3). The difference between $\alpha_n^{MOST}(z)$ and the observed $\alpha_n(z)$ cannot compensate for the zero β_n^{MOST} because $\alpha(z)$ and $\beta(z)$ describe different characteristics of $u_*(z)$ variations with $\bar{V}(z)$: $\alpha(z)$ is the rate of the $u_*(z)$ generation dominated by shear, and $\beta(z)$ is associated with $\bar{V}_s(z)$, which represents the required minimum $\bar{V}(z)$ for shear-generated turbulent mixing within the layer between height z and the surface that is strong enough to eliminate the influence of the atmospheric stratification on turbulence mixing.

We now investigate how the surface thermal condition affects $u_*(z)$ when $R_{net} \neq 0$. When $R_{net} \neq 0$, $\alpha(z)$ does not deviate significantly from its neutral value for $z \leq 1.5$ m, which confirms the existence of the near-neutral sublayer discussed in Sect. 4.5. At night when $R_{net} < 0$, the larger $\alpha(z)$ compared to its neutral value reflects the small monotonically decreasing stratification with increasing $\bar{V}(z)$ even when $\bar{V}(z)$ exceeds $\bar{V}_s(z)$. The relatively constant $\alpha(z)$ for $z \geq 20$ m for stable conditions suggests that the atmospheric stratification for $z \geq 20$ m does not change significantly during CASES-99. The increasing negative $\beta(z)$ for the stable case compared with its neutral value at a given z reflects the required increasing shear for overcoming the increasing $\Delta\bar{\theta}(z)$ with height to reach the strong mixing regime.

During daytime when $R_{net} > 0$, $\alpha(z)$ is smaller than its neutral value, and decreases with height while $\beta(z)$ becomes slightly positive and increases slightly with height (Fig. 13c). The relatively small deviations of $\alpha(z)$ and $\beta(z)$ from their neutral values compared to their nighttime deviations indicate that the contribution of thermally-generated turbulence to momentum transfer in the convective surface layer does not affect the $u_*(z) - \bar{V}(z)$, $u_*(z)$–$\bar{V}(z)$ relationship significantly even though the absolute value of R_{net} is much larger during daytime than at night.

We now discuss nighttime weak turbulent mixing under stable conditions when $\bar{V}(z) < \bar{V}_s(z)$. The observations in Figs. 4a and 4b indicate that unless turbulence at any height z is dominated by the strong top-down turbulent transport, $u_*(z)$ at a given z is normally in the stable regime below $u_{*s}(z)\bar{V}(z)/\bar{V}_s(z)$, which is schematically outlined by the dashed lines in Fig. 13a. In general, $u_*(z)$ in the outlined stable regime decreases with increasing $\Delta\bar{\theta}(z)$, and becomes smaller with increasing height due to the decoupling of turbulence between z and the surface. Because statistically $\bar{V}(z) > \bar{V}_s(z)$ occurs less frequently with increasing height, the percentage of $u_*(z)$ in the stable regime increases with height. The turbulence in the stable regime is generated by $\delta\bar{V}(z)/\delta z$ as well as directional shear; the length scale δz for shear generation of turbulence varies between zero and z, and may be smaller than the vertical resolution of observations. We cannot predict $u_*(z)$ in this regime well unless we understand the variation of δz. In addition, part of the shear-generated turbulence energy is used to increase TPE, which depends on the magnitude of the vertical temperature gradient, which in turn depends on the history of turbulent events in transporting the cold air from the surface to higher levels at night and the efficiency of surface cooling. Understanding the physical processes that lead to δz for turbulence generation and temporal variations of TKE and TPE in the interior of the atmosphere away from the surface are difficult, and more investigations are needed.

From the above analyses, the HOST of any TKE-related turbulent variable across the transition between the stable and near-neutral regimes at a height influenced by any surface type should have a similar pattern as the observed one here. However, the shape of the HOST depends on nighttime variations of $\alpha(z)$ and $\beta(z)$, where $\alpha(z)$ is influenced by both z_m and R_{net}, which in turn are influenced by surface properties, and $\beta(z)$ is related to $\bar{V}_s(z)$, which is related to the depth of the mixing layer as well as surface properties. When z_m over complex terrain is wind-direction dependent, $\alpha(z)$ can vary with wind direction; thus using wind from all directions may smear out the dramatic transition of any TKE-related variable between the stable and the near-neutral regimes as a function of $\bar{V}(z)$. In addition, if the atmospheric stratification is enhanced by local circulations in complex terrain, such as strong downslope winds associated with adiabatic warming, the HOST transition of any TKE-related variable may not be as well-defined as for level terrain.

5.2 Vertical variation of $\theta_*(z)$

As demonstrated in Sect. 4.3, $\theta_*(z)$, is approximately linearly related to the atmospheric stratification, $\Delta\bar{\theta}(z)$, for the convective and near-neutral surface layer, i.e., when $\Delta\bar{\theta}(z) \leq 0$ or $\Delta\bar{\theta}(z) > 0$ and $\bar{V}(z) > \bar{V}_s(z)$, which can be approximately expressed as

$$\theta_*(z) = \gamma(z)\Delta\bar{\theta}(z), \tag{15}$$

where $\gamma(z)$ is a coefficient that varies with z. Since Eq. 15 is valid when the surface layer approaches neutral as well as under unstable conditions as shown in Figs. 6b and 7c, the observed $\gamma(z)$ can be compared with the MOST bulk formula under neutral conditions,

$$\gamma_n^{MOST}(z) = \frac{\kappa}{\ln(z/z_h)}. \tag{16}$$

The observations in Fig. 13d show that $\gamma(z)$ decreases sharply with height near the surface and remains nearly constant above about 20 m, approaching the lower part of the mixed layer. Similar to the observed $\gamma(z)$, $\gamma_n^{MOST}(z)$ decreases with height, but the sharp decrease ceases around 10 m, and remains nearly constant for $z > 10$ m, which is different from the steady decrease of the observed $\gamma(z)$. As with z_m, changing z_h can only improve the fit of $\gamma_n^{MOST}(z)$ from one level to another near the surface. The non-constant $\theta_*(z)$ observed in Fig. 7d may also contribute to the discrepancy between the observed $\gamma(z)$ and $\gamma_n^{MOST}(z)$.

At night, the observations in Fig. 7a indicate that $\theta_*(z)$ varies nearly linearly with $\bar{V}(z)/\bar{V}_s(z)$ close to the surface. As z increases, $\theta_*(z)$ is near zero for weak $\bar{V}(z)/\bar{V}_s(z)$ and increases sharply with $\bar{V}(z)/\bar{V}_s(z)$ when $\bar{V}(z)/\bar{V}_s(z)$ approaches one. We find that when $\bar{V}(z) \leq \bar{V}_s(z)$, for example, at $\bar{V}(z)/\bar{V}_s(z) = 0.125$, $\theta_*(z)$ decreases steadily with height as does $\theta_*^{max}(z)$ (Fig. 13e). However the variation of $\theta_*(z)$ for a given $\bar{V}(z)/\bar{V}_s(z)$ at a given height is relatively large compared with that for $u_*(z)$ especially at large heights as the temperature variance depends on the history of turbulent heat transfer; i.e., the depletion of the cold air near the surface. Because $\Delta\bar{\theta}(z)$ is an internal parameter influenced by the external forcings of wind and variable surface temperature, which can be affected by surface properties such as soil type and moisture, and vegetation cover, as well as downward radiation, $\gamma(z)$ can be surface-dependent.

5.3 Limitations of MOST

The MOST bulk formulae are commonly believed to be valid near the surface, but the exact depth of the layer where MOST is valid, i.e., the MOST layer, is not clear in the literature, and is commonly assumed to be the bottom 10% of the ABL. Because of the existence of the near-neutral sublayer described in Sect. 4.5, to capture a range of stability conditions, Φ_m and Φ_h have to be estimated using observed $\partial\bar{V}(z)/\partial z$ and $\partial\bar{\theta}(z)/\partial z$ at a height not too close to the surface even though MOST correctly describes the neutral stratification as $z/L \to 0$ at $z \to 0$. As the observed $\gamma(z)$, which is valid for both neutral and unstable conditions, and $\alpha_n(z)$ vary with height near the surface, determination of z_m and z_h based on Eqs. 12 and 16, respectively, may be observation-height dependent even when the turbulent mixing at height z is fully coupled to the surface.

Comparison between the observed $\partial\bar{V}(z)/\partial z$ and $\bar{V}(z)/z$ indicates that the two are linearly related near the surface, and both decrease with height for all stabilities (Fig. 14); however because the bulk shear $\bar{V}(z)/z$ decreases gradually with height, $\bar{V}(z)/z > \partial\bar{V}(z)/\partial z$ unless the level z is above the near-neutral sublayer and wind speed is small such that the atmospheric stability at z is significant. Turbulent mixing in response to the larger shear between $\bar{V}(z)/z$ and $\partial\bar{V}(z)/\partial z$ is demonstrated in S12. The lack of dependence of the nighttime V_{TKE} on $\partial\bar{V}(z)/\partial z$ for $z > 5$ m in S12 clearly suggests that the variation of $\partial\bar{V}(z)/\partial z$ is not the driving factor for turbulence generation, but a consequence of momentum transfer by large eddies constrained by the turbulence energy balance within the layer between height z and the surface.

Using local vertical gradients of mean variables, such as $\partial\bar{V}(z)/\partial z$, which is affected by the surface, to capture turbulence variables such as $u_*(z)$ over a finite vertical scale, δz, relies on the establishment of an approximate relationship between $\partial\bar{V}(z)/\partial z$ and $\delta\bar{V}(z)/\delta z$, which inevitably is height-dependent. As a result, the performance of the relationship between $u_*(z)$ and $\partial\bar{V}(z)/\partial z$ deteriorates when the relationship is applied at a height that deviates from the height where the approximate relationship between $\partial\bar{V}(z)/\partial z$ and $\delta\bar{V}(z)/\delta z$ is established. Applying the MOST bulk formulae above 10 m under all stability conditions would lead to systematic underestimation of $u_*(z)$ and $\theta_*(z)$ mainly due to the underestimation of $\alpha_n(z)$ and $\gamma(z)$ by applying $\alpha_n^{MOST}(z)$ and $\gamma_n^{MOST}(z)$ (Fig. 15), for which stability functions can only modify turbulence intensity from their neutral values at a given height, and cannot correct for any systematic biases of turbulence variations with height under the neutral condition. The assumed constancy of $u_*(z)$ and $\theta_*(z)$ in MOST partly contributes to the underestimation of $\alpha_n(z)$ and $\gamma(z)$.

At a height of 0.5 m, the MOST bulk formula systematically overestimates u_* for large u_* even though $\alpha_n^{MOST}(z)$ and $\beta_n^{MOST}(z)$ agree reasonably well with the observed $\alpha_n(z)$ and $\beta_n(z)$. The overestimate under strong winds is likely due to the application of the stability functions developed above the near-neutral sublayer to the near-neutral sublayer at 0.5 m. Comparison between the estimated and observed $u_*(z)$ and $\theta_*(z)$ with the stability functions described in Beljaars and Holtslag (1991) (Fig. 15) suggests that the MOST layer is approximately below 10 m and above O(1) m throughout the diurnal cycle.

The relatively poor performance of the MOST bulk formula for daytime $\theta_*(z)$ even in the MOST layer compared with that for $u_*(z)$ is due to the relatively large departure between the observed $\gamma(z)$ and $\gamma_n^{MOST}(z)$. Fundamentally $\bar{V}(z)$ and $\bar{\theta}(z)$ play different roles in mechanical and thermal generation of turbulence. Shear-generated u_* is directly associated with the vertical variation of $\bar{V}(z)$ and the momentum sink at the surface, and $\bar{V}(z)$ is forced by horizontal pressure gradients. In contrast, $\theta_*(z)$ is related to $\Delta\bar{\theta}(z)$ only under unstable and near-neutral conditions, and $\Delta\bar{\theta}(z)$ is an internal parameter dependent on heat transfer by thermally- or mechanically-generated turbulent mixing. Thus, the observed $\alpha_n(z)$ varies approximately logarithmically with height while $\gamma(z)$ decreases with height at a rate less than the logarithmic decrease predicted by $\gamma_n^{MOST}(z)$. Therefore, the relationships between $\Delta\bar{\theta}(z)$ and $\theta_*(z)$ and between $\bar{V}(z)$ and $u_*(z)$ are not similar for all stabilities as assumed in MOST.

The fundamental issues that limit the validity of MOST in a shallow layer are, 1) its inability to capture the generation of large non-local turbulent eddies by relating turbulence intensity to local vertical gradients, and 2) the neglect of interactions between turbulent mixing and the vertical potential temperature gradient when the vertical potential temperature gradient depends on turbulent mixing. The former issue goes beyond MOST. The assumption that the magnitude of the turbulent momentum transfer is related to $\partial\bar{V}(z)/\partial z$ when large eddies are actually generated by $\bar{V}(z)/z$ leads to, for example, counter-gradient fluxes (Garratt, 1992) or negative viscosity (Starr, 1968) when $\bar{V}(z)/z$ and $\partial\bar{V}(z)/\partial z$ have different signs. In other words, counter-gradient fluxes represent turbulent transport by large eddies when the vertical difference of mean quantity over the deep layer has an opposite sign from its local gradient at z. The importance of counter-gradient fluxes in the ABL especially under convective conditions has been recognized in the literature for decades. Fundamentally, the validity of the Boussinesq hypothesis requires that the turbulent mixing length is small compared to the scale of vertical variations of mean variables (Tennekes and Lumley, 1972; Schmitt, 2007). Violation of the assumed similarity between molecular diffusion and turbulent mixing has been investigated by Hamba (2005) and Sanderse et al. (2011) especially for turbulent mixing near a wall under near-neutral conditions.

6 Summary

We extend the work of S12 on the observed nighttime turbulence transition with $\bar{V}(z)$ and further investigate turbulent mixing in the CASES-99 60-m atmospheric layer above the surface by examining the diurnal variation of $u_*(z)$ and $\theta_*(z)$. Based on the data analyses, we propose the HOST hypothesis to generalize the explanation for the observed diurnal variation of $u_*(z)$ and $\theta_*(z)$: the magnitude of a TKE-related variable is dominated by large coherent eddies of finite vertical scale δz determined by the turbulence energy generation, such as by positive buoyancy or shear, and the turbulence energy partition between TKE and TPE within the layer of depth δz (Fig. 1). Because of the connection between TKE and TPE through buoyancy fluxes, thermally-generated turbulence from positive surface buoyancy enhances not only TPE but also TKE; mechanically-generated turbulence from shear enhances not only TKE but also TPE and the partition between the two varies with the diurnal variation of the surface heating/cooling. The HOST hypothesis explains the observed transition of a TKE-related variable, such as V_{TKE}, σ_w, or $u_*(z)$, from their stable to near-neutral regimes at night, the stronger dependence of $\theta_*(z)$ on wind speed rather than $\Delta\bar{\theta}(z)$ at night, the dependence of daytime $\theta_*(z)$ on $\Delta\bar{\theta}(z)$, and the enhancement of $u_*(z)$ by thermally-generated turbulent mixing during daytime.

The analyses suggest that the limitations of the MOST bulk formulae result from their not including turbulent eddies of finite sizes by using local vertical gradients of mean variables especially under strong mixing conditions such as near-neutral and unstable conditions, and the lack of dynamic coupling between TKE and TPE. The assumptions of the relationship between the magnitude of turbulence and local vertical gradients, such as $\partial\bar{V}(z)/\partial z$ and $\partial\bar{\theta}(z)/\partial z$, and the analogy between wind speed and temperature in their relationships with $u_*(z)$ and $\theta_*(z)$ for all stabilities in MOST are of limited validity, and the MOST bulk formulae are applicable only within a thin layer (Fig. 1). During CASES-99, the MOST layer is approximately between O(1) m and 10 m.

While the HOST hypothesis emphasizes the contribution of large coherent eddies and the need for considering the coupling between the turbulence kinetic and potential energies in the turbulence generation layer for capturing variations of turbulence intensity, the HOST hypothesis does not invalidate the energy and heat balance at a point in space. However, this balance can be a consequence of turbulent transport by large coherent eddies.

Acknowledgements The authors thank three anonymous reviewers for their helpful comments, and acknowledge the field support from the Earth Observing Laboratory of the National Center for Atmospheric Research. Larry Mahrt received support from Grant AGS-1115011 from the National Science Foundation. The University Corporation for Atmospheric Research manages the National Center for Atmospheric Research under sponsorship by the National Science Foundation. Any opinions, findings and conclusions, or recommendations expressed in this publication are those of the authors and do not necessarily reflect the views of the National Science Foundation.

References

Acevedo OC, Fitzjarrald DR (2003) In the core of the night-effects of intermittent mixing on a horizontally heterogeneous surfaces. Boundary-Layer Meteorol 106:1–33

Andreas EL, Hicks BB (2002) Comments on “Critical test of the validity of Monin-Obukhov similarity during convective conditions.”. J Atmos Sci 59:2605–2607

Baas P, Steeneveld GJ, van de Wiel BJH, Holtslag AAM (2006) Exploring self-correlation in flux-gradient relationships for stably stratified conditions. Q J R Meteorol Soc 63:3045–3054

Banta RM (2008) Stable-boundary-layer regimes from the perspective of the low-level jet. Acta Geophys 56:58–87, DOI 10.2478/s11600-007-0049-8

Banta RM, Pichugina YL, Newsom RK (2003) Relationship between low-level jet properties and turbulence kinetic energy in the nocturnal stable boundary layer. J Atmos Sci 60:2549–2555

Beljaars ACM, Holtslag AAM (1991) Flux parameterization over land surfaces for atmospheric models. J Appl Meteorol 30:327–341

Bonin TA, Blumberg WG, Klein PM, Chilson PB (2015) Thermodynamic and turbulence characteristics of the Southern Great Plains nocturnal boundary layer under differing turbulent regimes. Boundary-Layer Meteorol 157:1–2

Boussinesq J (1877) Essai sur la théorie des eaux courantes. Mémoires présentés par divers savants à l’Académie des Sciences 23(1):1–680

Caulfield CP, Kerswell RR (2001) Maximal mixing rate in turbulent stably stratified Coutte flow. Phys Fluids 13:894–900

Etling D, Brown R (1993) Roll vortices in the planetary boundary layer: A review. Boundary-Layer Meteorol 65:215–248

Garratt JR (1992) The Atmospheric Boundary Layer. Cambridge University Press, UK, 316 pp

Hamba F (2005) Nonlocal analysis of the Reynolds stress in turbulent shear flow. Phys Fluids 17(11):115,102

Hicks BB (1978) Some limitations of dimensional analysis and power laws. Boundary-Layer Meteorol 14:567–569

Högström U (1996) Review of some basic characteristics of the atmospheric surface layer. Boundary-Layer Meteorol 78(3-4):215–246

Högström U, Hunt JCR, Smedman AS (2002) Theory and measurements for turbulence spectra and variances in the atmospheric neutral surface layer. Boundary-Layer Meteorol 103:101–124

Holliday D, McIntyre ME (1981) On potential energy density in an incompressible, stratified fluid. J Fluid Mech 107:221–225

Hopfinger EJ (1987) Turbulence in stratified fluids: A review. J Geophys Res 92(C5):5287–5303

Howell J (1995) Identifying sudden changes in data. Mon Weather Rev 123(4):1207–1212

Howell J, Mahrt L (1994) An adaptive multiresolution data filter: Applications to turbulence and climatic time series. J Atmos Sci 51(4):2165–2178

Howell JF, Sun J (1999) Surface-layer fluxes in stable conditions. Boundary-Layer Meteorol 90:495–520

Von Kármán T (1930) Mechanische Ähnlichkeit und turbulenz (Mechanical Similarity and Turbulence). Nachr Ges Wiss Göttingen Math Phys Klasse

King JC, Mobbs SD, Edwards NR (1994) Surface boundary conditions in stably-stratified environmental flows. In: Castro IP, Rochliff NJ (eds) Stably Stratified Flows: Flow and Dispersion over Topography, Institute of Mathematics and Its Applications, University of Surrey; Oxford University Press, pp 93–103

Klipp CL, Mahrt L (2004) Flux-gradient relationship, self-correlation and intermittency in the stable boundary layer. Q J R Meteorol Soc 130:2087–2103

Lenschow DH, Zhang SF, Stankov BB (1988) The stably stratified boundary layer over the Great Plains I: Mean and turbulence structure. Boundary-Layer Meteorol 42:95–121

Lin JT, Pao YH (1979) Wakes in stratified fluids. Ann Rev Fluid Mech 11:317–338

Lindborg E (2006) The energy cascade in a strongly stratified fluid. J Fluid Mech 550:207–242

Mahrt L (2007) The influence of nonstationarity on the turbulent flux-gradient relationship for stable stratification. Boundary-Layer Meteorol 125:245–264

Mahrt L (2008) Bulk formulation of surface fluxes extended to weak-wind stable conditions. Q J R Meteorol Soc 134:1–10

Mahrt L (2009) Characteristics of submeso winds in the stable boundary layer. Boundary-Layer Meteorol 130:1–14

Mahrt L, Sun J, Blumen W, Delany T, Oncley S (1998) Nocturnal boundary-layer regimes. Boundary-Layer Meteorol 88:255–278

Mahrt L, Thomas C, Richardson S, Seaman N, Stauffer D, Zeeman M (2013) Non-stationary generation of weak turbulence for very stable and weak-wind conditions. Boundary-Layer Meteorol 147(2):179–199

Mahrt L, Sun J, Stauffer D (2015) Dependence of turbulent velocities on wind speed and stratification. Boundary-Layer Meteorol 155(1):55–71

Martins HS, Sá LD, Moraes OL (2013) Low level jets in the Pantanal wetland nocturnal boundary layer–case studies. Amer J Environ Eng 3(1):32–47

McNaughton K (2009) The rise and fall of Monin-Obukhov theory. AsiaFlux Newsletter 30:1–22

Monin AS, Obukhov AM (1954) Basic laws of turbulent mixing in the atmosphere near the ground. Trudy Geofiz Inst AN SSSR 24:163–187

Obukhov AM (1946) Turbulence in an atmosphere with a non-uniform temperature. Trudy Instituta Teoreticheskio Geofiziki AN SSSR 1:95–115.

Ostrovsky L, Troitskaya YI (1987) A model of turbulent transfer and dynamics of turbulence in a stratified shear-flow. Izvestiya Akademii Nauk Sssr Fizika Atmosfery I Okeana 23(10):1031–1040

Peña A, Gryning SE, Mann J (2010) On the length-scale of the wind profile. Q J R Meteorol Soc 136:2119–2131

Poulos GS, Blumen W, Fritts DC, Lundquist JK, Sun J, Burns SP, Nappo C, Banta R, Newsom R, Cuxart J, Terradellas E, Balsley B, , Jensen M (2002) CASES-99—A comprehensive investigation of the stable nocturnal boundary layer. Bull Amer Meteor Soc 83:555–581

Prandtl L (1925) Report on investigation of developed turbulence. Tech. rep., National Advisory Committee for Aeronautics, Technical Memorandum No. 1231

Sanderse S, van der Pijl SP, Koren B (2011) Review of computational fluid dynamics for wind turbine wake aerodynamics. Wind Energy 14:799–819

Schmitt F (2007) About Boussinesq's turbulent viscosity hypothesis: Historical remarks and a direct evaluation of its validity. Comptes Rendus Mecanique 335(9/10):617–627

Starr VP (1968) Physics of Negative Viscosity Phenomena. McGraw-Hill Book Company

Stull RB (1984) Transilient turbulence theory. Part I: The concept of eddy-mixing across finite distances. J Atmos Sci 41(23):3351–3367

Sun J (2007) Tilt corrections over complex terrain and their implication for CO_2 transport. Boundary-Layer Meteorol 124:143–159

Sun J (2011) Vertical variations of the mixing lengths during CASES-99. J Appl Meteor Clim 50:2030–2041

Sun J, Mahrt L (1995) Determination of surface fluxes from the surface radiative temperature. J Atmos Sci 52(8):1096–1106

Sun J, Massman W (1999) Ozone transport during the California Ozone Deposition Experiment. J Geophys Res 104(D10):11,939–11,948

Sun J, Esbensen SK, Mahrt L (1995) Estimation of surface heat flux. J Atmos Sci 52(17):3162–3171

Sun J, Burns SP, Lenschow DH, Banta R, Newsom R, Coulter R, Frasier S, Ince T, Nappo C, Cuxart J, Blumen W, Lee X, Hu XZ (2002) Intermittent turbulence associated with a density current passage in the stable boundary layer. Boundary-Layer Meteorol 105:199–219

Sun J, Burns SP, Delany AC, Oncley SP, Horst TW, Lenschow DH (2003) Heat balance in nocturnal boundary layers during CASES-99. J Appl Meteorol 42:1649–1666

Sun J, Mahrt L, Banta RM, Pichugina YL (2012) Turbulence regimes and turbulence intermittency in the stable boundary layer during CASES-99. J Atmos Sci 69:338–351

Sun J, Lenschow DH, Mahrt L, Nappo C (2013) The relationships among wind, horizontal pressure gradient, and turbulent momentum transport during CASES-99. J Atmos Sci 70:3397–3414

Sun J, Mahrt L, Nappo C, Lenschow DH (2015) Wind and temperature oscillations generated by wave-turbulence interactions in the stably stratified boundary layer. J Atmos Sci 72:1484–1503

Tennekes H, Lumley HL (1972) A First Course in Turbulence. The MIT Press

van de Wiel B, Moene A, Steeneveld G, Hartogensis O, Holtslag A (2007) Predicting the collapse of turbulence in stably stratified boundary layers. Flow Turbul Combust 79(3):251–274

van de Wiel BJH, Moene AF, Jonker HJJ, Baas P, Basu S, Donda JMM, Sun J, Holtslag AAM (2012) The minimum wind speed for sustainable turbulence in the nocturnal boundary layer. J Atmos Sci 69:3116–3127

Wilczak JM, Oncley SP, Stage SA (2001) Sonic anemometer tilt correction algorithms. Boundary-Layer Meteorol 99(1):127–150

Williams A, Hacker J (1992) The composite shape and structure of coherent eddies in the convective boundary layer. Boundary-Layer Meteorol 61(3):213–245

Zilitinkevich SS (1995) Non-local turbulent transport: pollution dispersion aspects of coherent structure of convective flows. WIT Trans Ecol Envir 6:53–60

Zilitinkevich SS, Hunt J, Esau IN, Grachev A, Lalas D, Akylas E, Tombrou M, Fairall C, Fernando H, Baklanov A, et al. (2006) The influence of large convective eddies on the surface-layer turbulence. Q J R Meteorol Soc 132(618):1426–1456

Zilitinkevich SS, Elperin T, Kleeorin N, Rogachevskii I (2007) Energy- and flux-budget (EFB) turbulence closure model for stably stratified flows. Part I:

Steady-state, homogeneous regimes. Boundary-Layer Meteorol 125:167–191

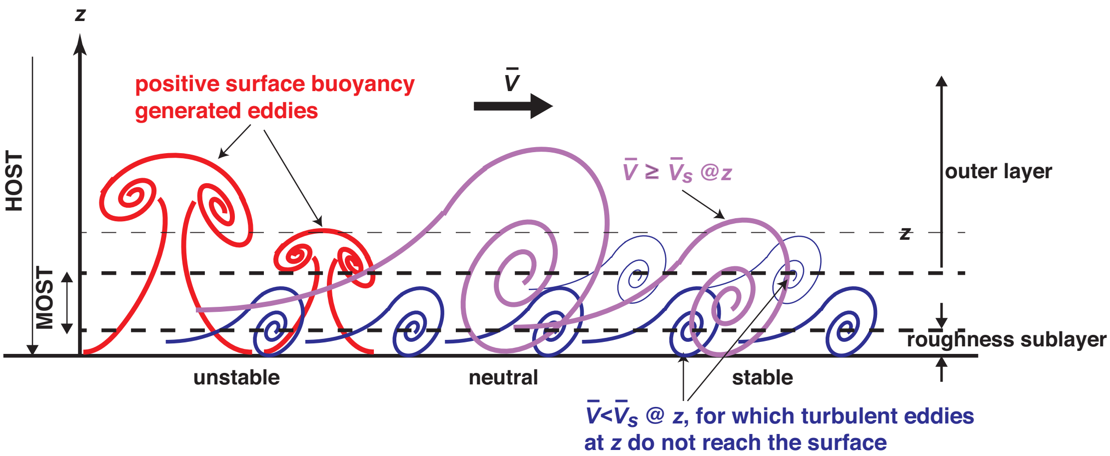

Fig. 1 Schematic illustration showing the thin layer where MOST is valid (between the two thick dashed lines), and the characteristic sizes of turbulent eddies described in the HOST hypothesis. Turbulent eddies in purple and blue are generated by shear $\delta \bar{V}(z)/\delta z$ for $\delta z = z$ and $\delta z < z$, respectively. The thick and thin blue eddies represent the situations when turbulent eddies are attached to the surface but the shallow turbulence layer is below height z, and when turbulent eddies are generated by elevated shear above the surface; in both situations, turbulent eddies at z do not reach the surface. Turbulent eddies in red represent those generated by positive buoyancy from heated surface.

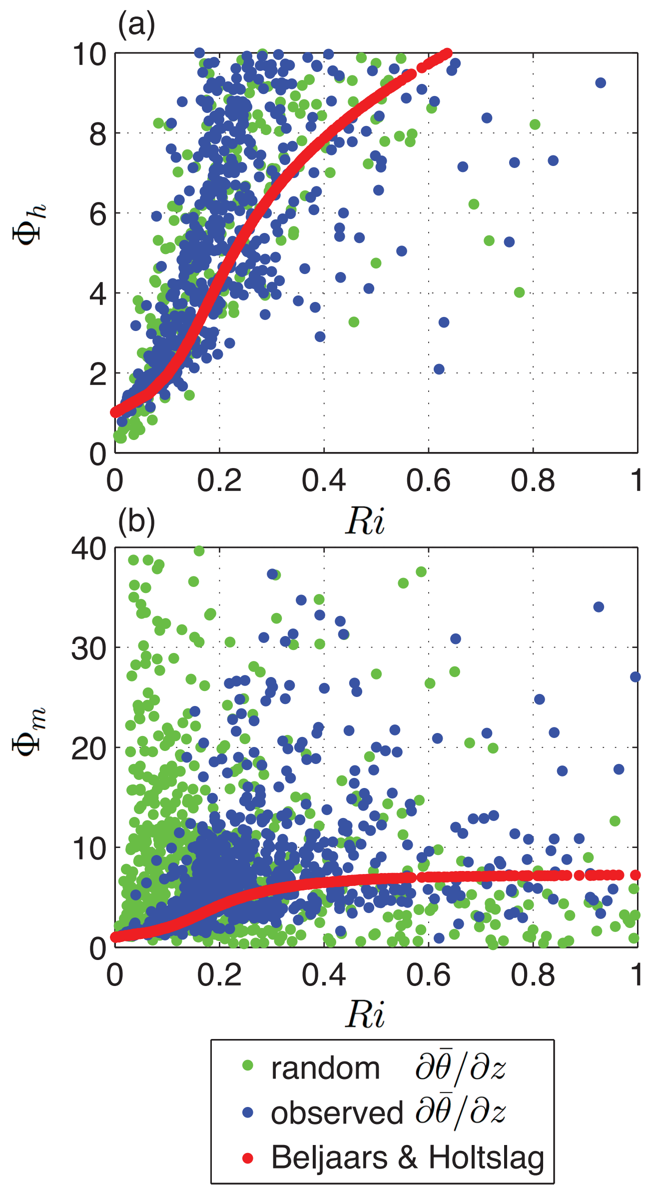

Fig. 2 Relationship between the 5-min Ri and (a) Φ_m, and (b) Φ_h at $z = 5$ m, where the blue and green dots are values of observed and randomly-generated $\partial\bar{\theta}/\partial z$ in the calculations, respectively. The red dots are calculated using the stability functions from Beljaars and Holtslag (1991).

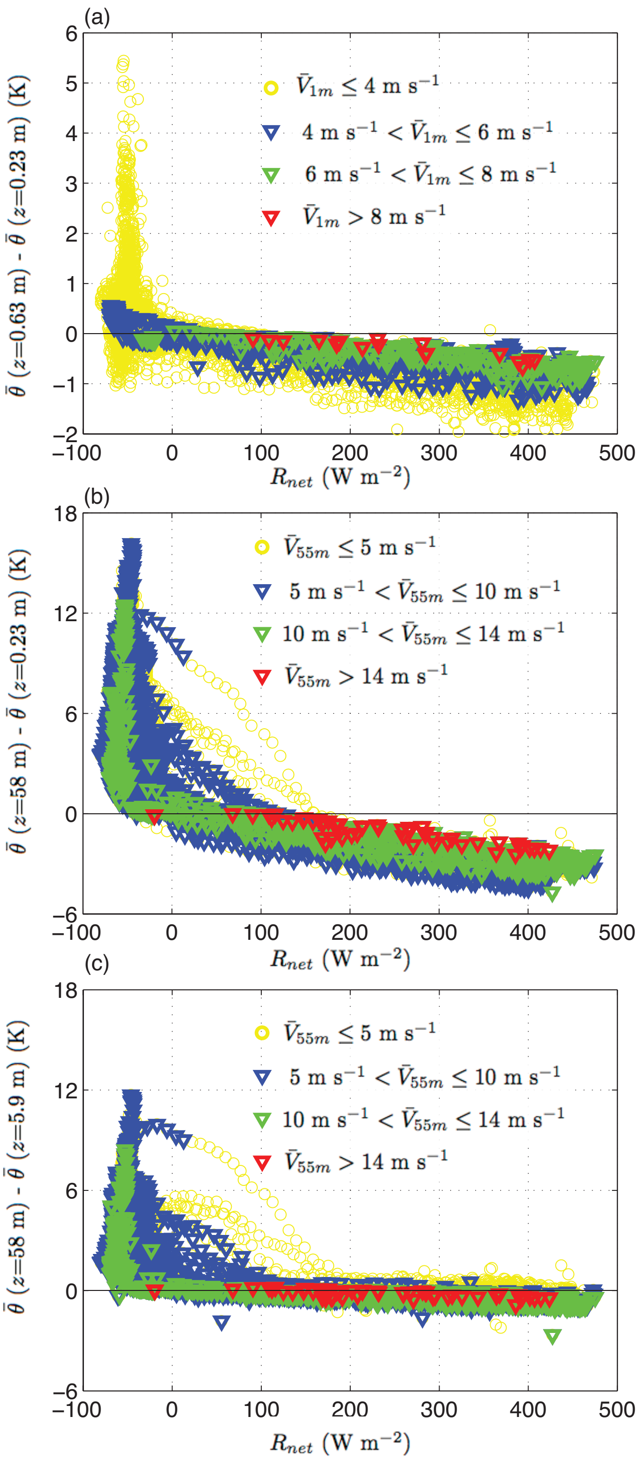

Fig. 3 Observed relationship between the net radiation (R_{net}) and the vertical potential temperature difference as a function of different wind-speed ranges for three layers: (a) between 0.63 m and 0.23 m, (b) between 58 m and 0.23 m, and (c) between 58 m and 5.9 m. Each symbol represents a 5-min average. The nighttime data are characterized by negative R_{net}.

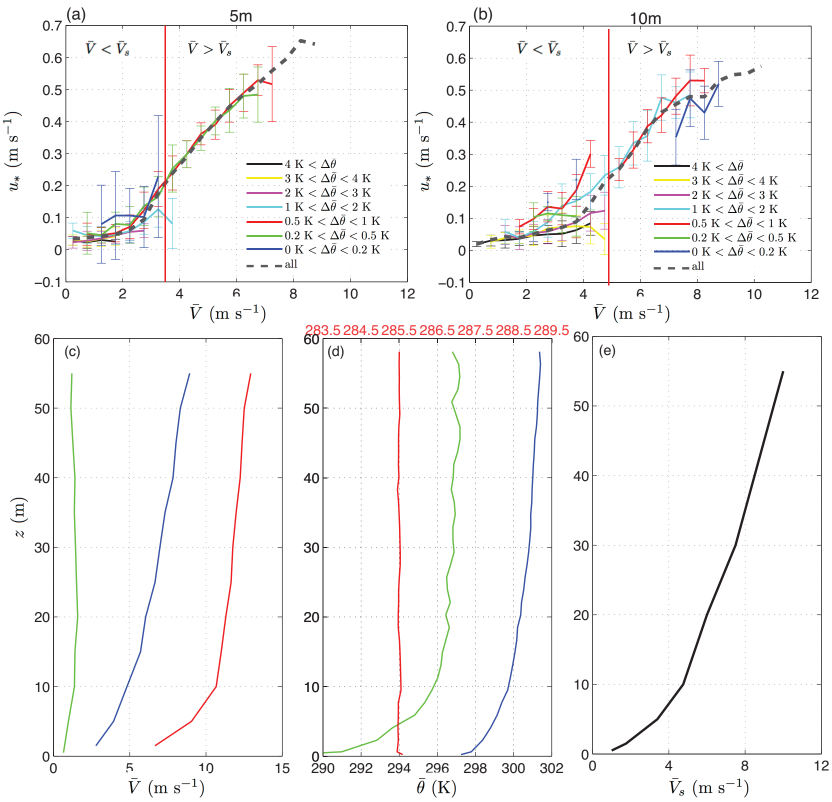

Fig. 4 Composite nighttime relationship between $\bar{V}(z)$ and $u_*(z)$ as a function of $\Delta\bar{\theta}(z)$ at, (a) 5 m, and (b) 10 m based on the 5-min dataset. Each wind speed bin of 0.5 m s^{-1} has at least five points. The black dashed line in (a) and (b) is the average of all the nighttime data, i.e., the HOST for $u_*(z)$. The red vertical line extending from top to bottom in (a) and (b) represents the threshold wind for the height identified by S12. $\Delta\bar{\theta}(z)$ for $\bar{V}(z) > \bar{V}_s(z)$ is < 1 K at 5 m and < 2 K at 10 m. The three $\bar{\theta}(z)$ profiles in (d) correspond to the three wind-speed profiles in (c) in the same colours. The temperature scale for the red $\bar{\theta}(z)$ profile in (d) is on the top, and for the green and blue profiles are on the bottom. The threshold wind speed $\bar{V}_s(z)$ as a function of height is shown in (e).

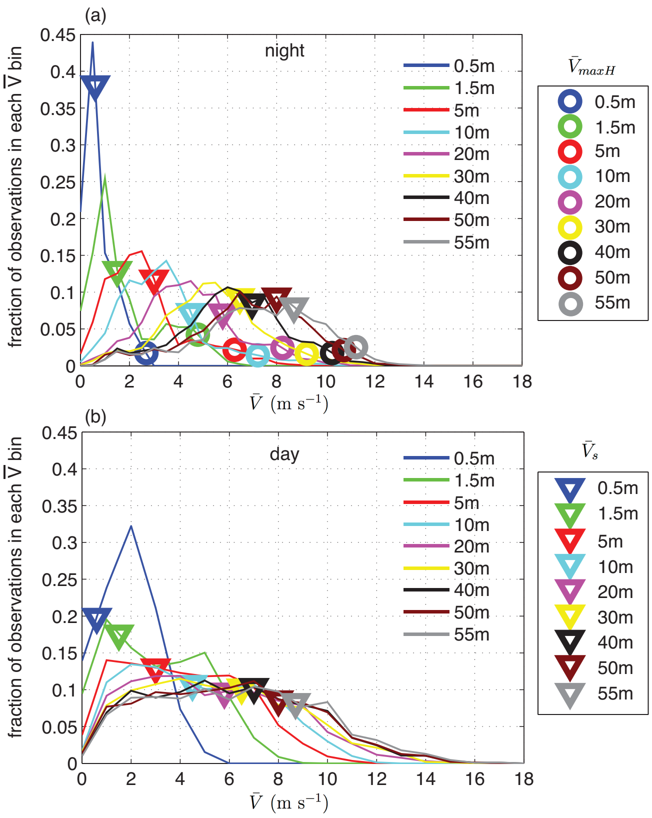

Fig. 5 (a) Nighttime and (b) daytime fractions of the 5-min observations as functions of wind speed $\bar{V}(z)$ within each 1 m s^{-1} bin for daytime and each 0.5 m s^{-1} bin for nighttime at the nine sonic anemometer heights, where the threshold wind $\bar{V}_s(z)$ at each level is marked with a triangle of the same colour. In addition, $\bar{V}(z)$ at which the nighttime maximum downward $\overline{w'\theta'}(z)$ occurs, $\bar{V}_{maxH}(z)$, is marked with a circle of the same colour in (a). Because $\bar{V}_s(z)$ marks the transition between stable and near-neutral conditions, it is used only as a reference in (b).

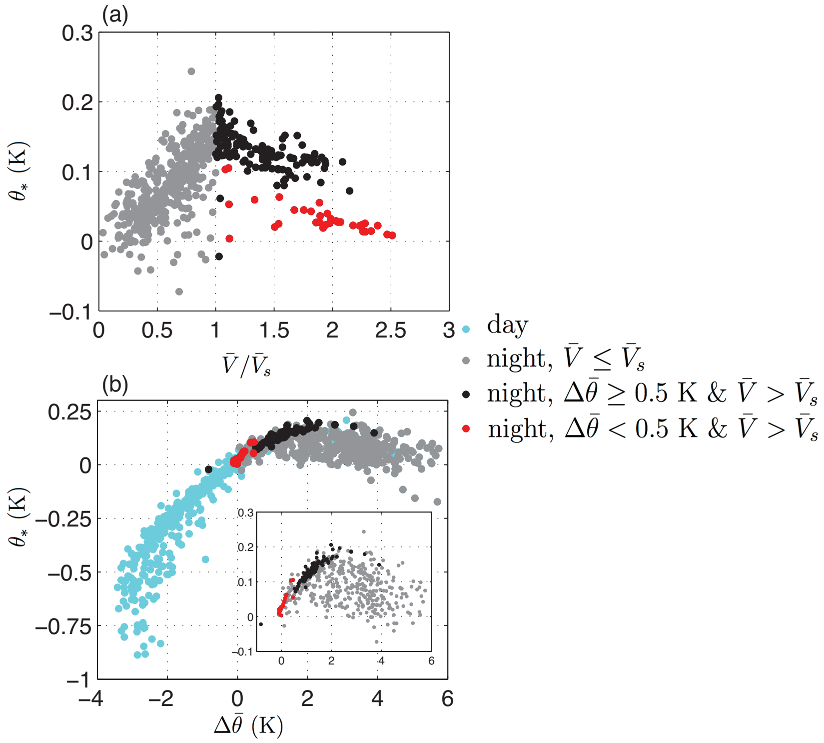

Fig. 6 The observed relationship at 5 m, (a) between $\theta_*(z)$ and $\bar{V}(z)/\bar{V}_s(z)$ at night, and (b) between $\theta_*(z)$ and the bulk potential temperature difference, $\Delta\bar{\theta}(z)$, throughout the diurnal cycle, where the inset is the enlarged nighttime relationship.

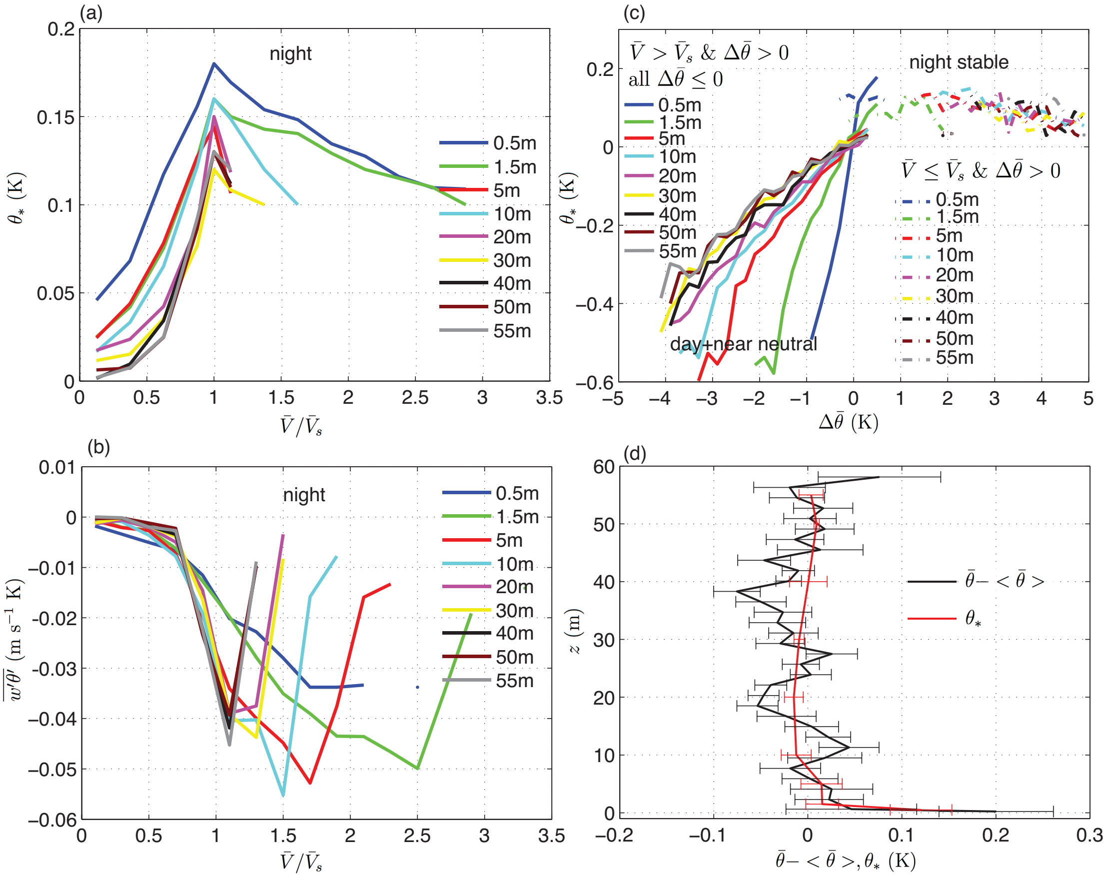

Fig. 7 Composite nighttime (a) $\theta_*(z)$ and (b) heat fluxes $\overline{w'\theta'}(z) = -u_*(z)\theta_*(z)$ as functions of $\bar{V}(z)/\bar{V}_s(z)$. (c) Composite $\theta_*(z)$ as a function of the bulk temperature difference $\Delta\bar{\theta}(z)$ for the daytime ($\Delta\bar{\theta}(z) \le 0$) and the near-neutral at night ($\Delta\bar{\theta}(z) > 0$ and $\bar{V}(z) > \bar{V}_s(z)$) (solid lines), and for the nighttime stable condition ($\Delta\bar{\theta}(z) > 0$ and $\bar{V}(z) \le \bar{V}_s(z)$) (dot-dashed lines). (d) The composite profiles of $\theta_*(z)$ and $\bar{\theta}(z)- < \bar{\theta}(z) >$ for -0.5 K $< \Delta\bar{\theta}(z) < 0$ K, where $< \bar{\theta}(z) >$ is the vertically averaged $\bar{\theta}(z)$. The removal of the vertically averaged $\bar{\theta}(z)$ results in easy comparison between the vertical variations of $\theta_*(z)$ and $\bar{\theta}(z)$.

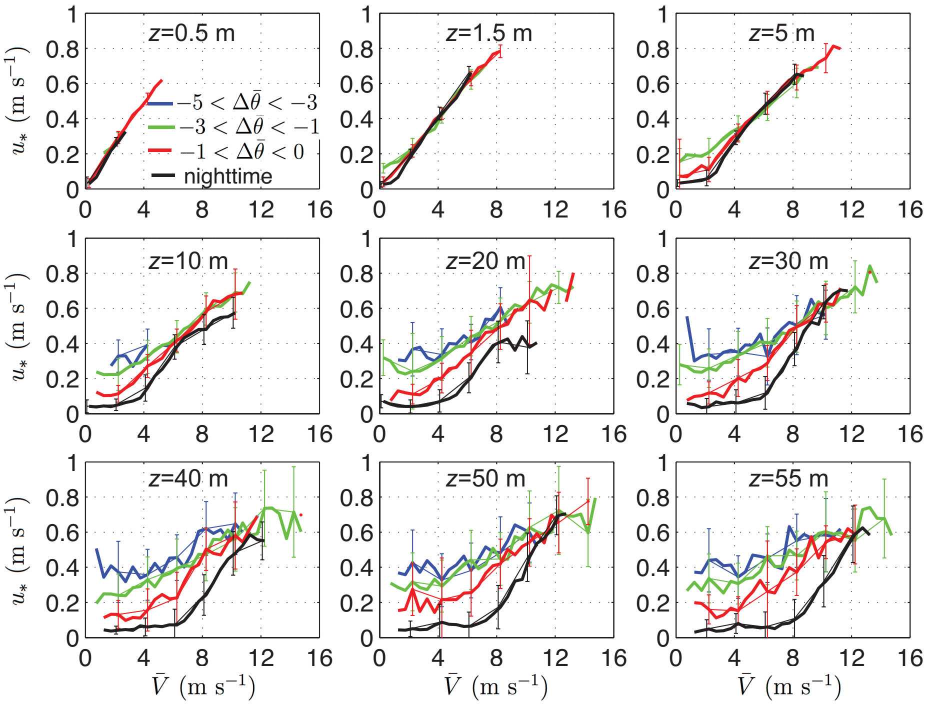

Fig. 8 Composite daytime relationships between $u_*(z)$ and $\bar{V}(z)$ compared to their averaged nighttime relationship from the entire CASES-99 30-min dataset at nine observation heights. The daytime relationship is further subdivided into three ranges of the bulk temperature difference $\Delta\bar{\theta}(z) = \bar{\theta}(z) - \bar{\theta}_0$ in K. The thin vertical lines represent the standard deviations within each 4 m s^{-1} $\bar{V}(z)$ bin.

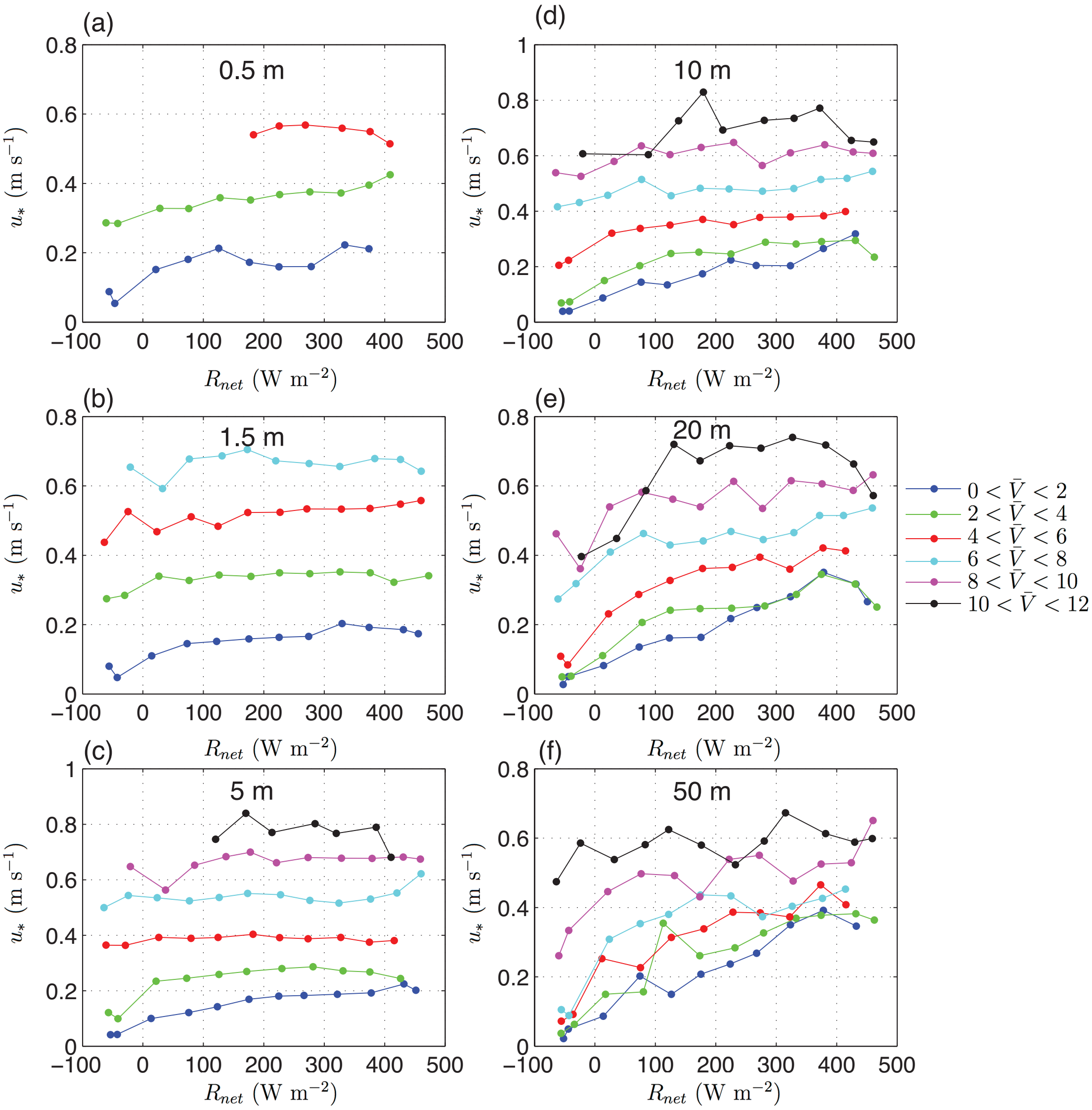

Fig. 9 Variations of $u_*(z)$ with net radiation R_{net} for different wind-speed ranges in m s^{-1} at the labelled observation heights.

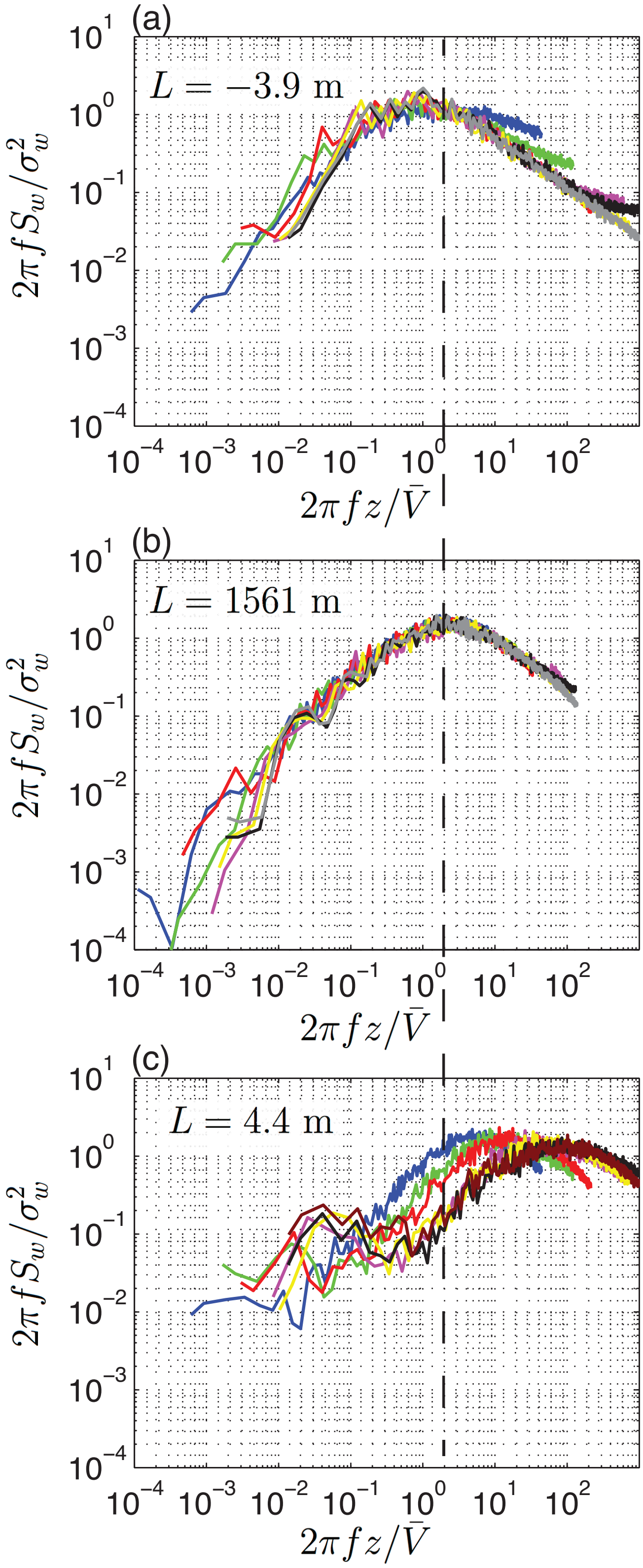

Fig. 10 Normalized vertical velocity w power spectra $S_w(z)$, $2\pi f S_w(z)/\sigma_w^2(z)$, as functions of normalized frequency $2\pi f z/\bar{V}(z)$ at eight observation heights for three stability conditions represented by the Obukhov length ($L = -3.9$ m from 1600-2000 UTC on 10 October, $L = -1561$ m from 0400-0800 UTC on 17 October, and $L = 4.4$ m from 0000-0400 UTC on 5 October), where $\sigma_w(z)$ is the standard deviation of w. The spectra are calculated using the data recorded at 20 samples s^{-1} at all observation heights except at 20 m in (c) due to sonic anemometer problems. (b) and (c) are selected for $\bar{V}(z) > \bar{V}_s(z)$ and $\bar{V}(z) < \bar{V}_s(z)$, respectively. The vertical dashed line marks $2\pi f z/\bar{V}(z) = 2$ where $2\pi f S_w(z)/\sigma_w^2(z)$ reaches its maximum in (b).

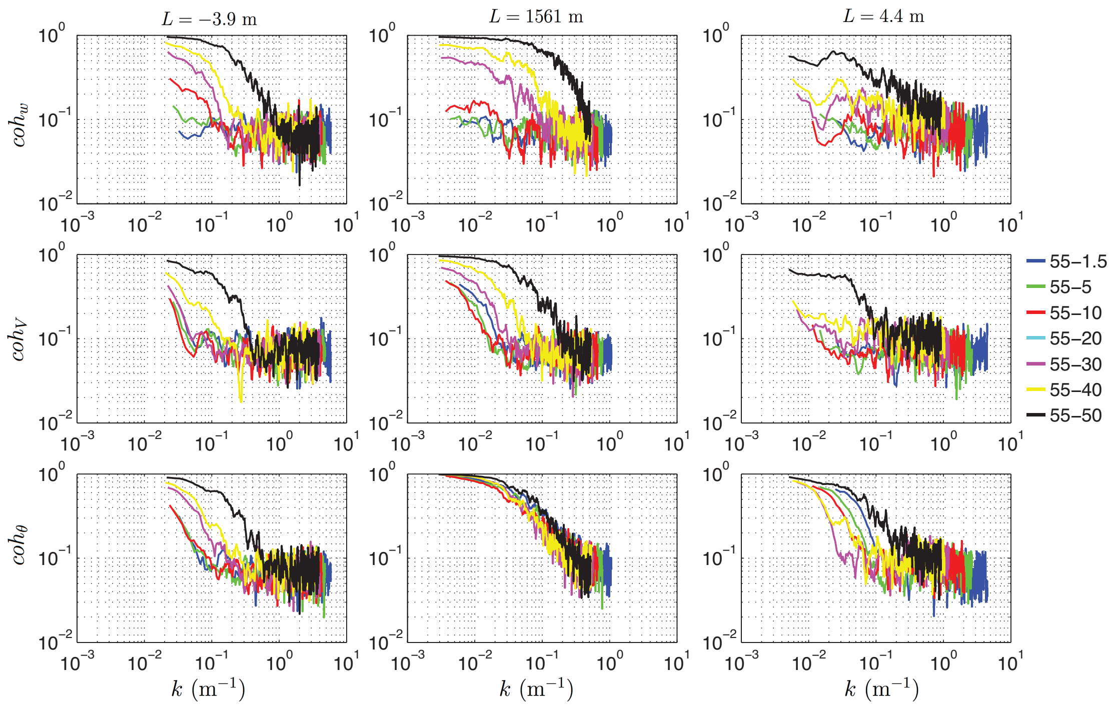

Fig. 11 Vertical coherences of vertical velocity w (coh_w, top row), wind speed V (coh_V, middle row), and potential temperature θ (coh_θ, bottom row) between 55 m and the successive underlying sonic anemometer heights as functions of wavenumber (k) at the underlying-height for the same three stability cases in Fig. 10, where the Obukhov length is labelled at the top of each column.

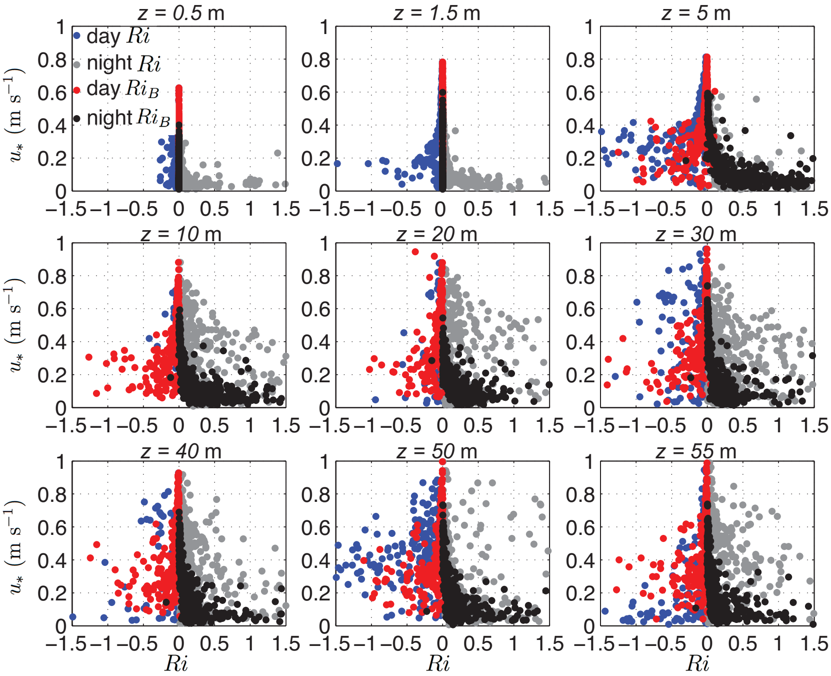

Fig. 12 Daytime and nighttime 30-min $u_*(z)$ values as a function of the bulk Richardson number Ri_B and the local gradient Richardson number Ri at the nine observation heights.

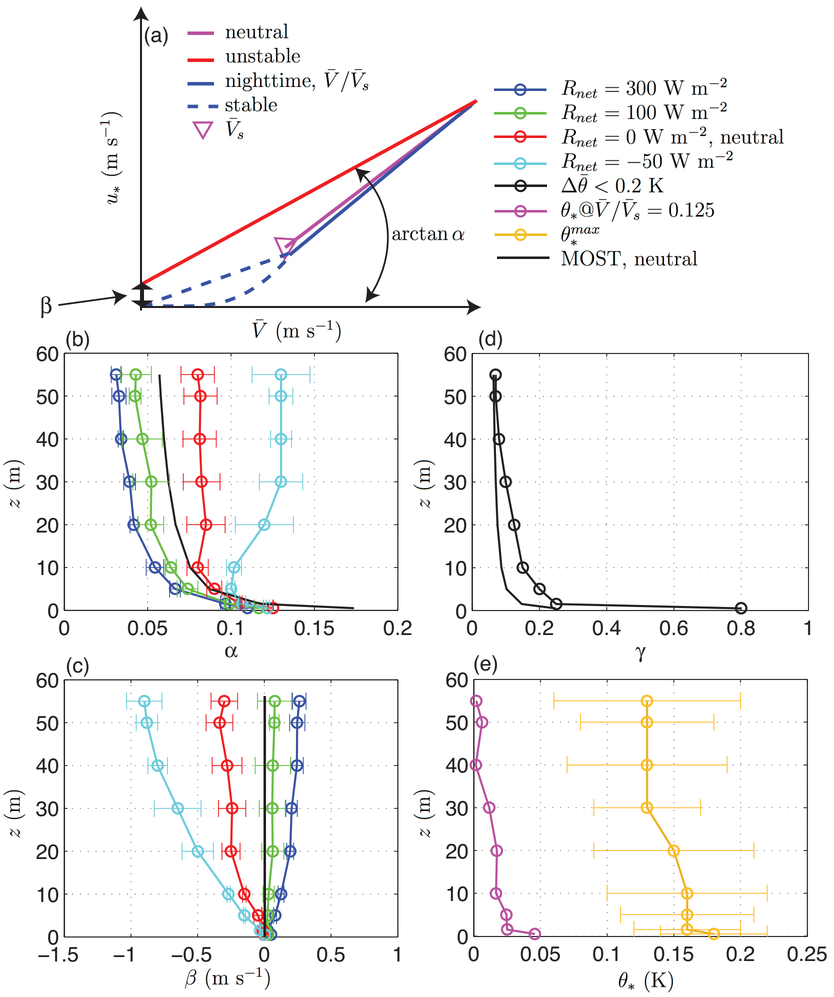

Fig. 13 The observed (b) $\alpha(z)$ and (c) $\beta(z)$ used in the relationship $u_*(z) = \alpha(z)\bar{V}(z) + \beta(z)$ (schematically illustrated in (a)) for various R_{net} values; (d) the observed $\gamma(z)$ in describing the daytime and near-neutral $\theta_*(z) = \gamma(z)\Delta\bar{\theta}(z)$, and (e) the observed $\theta_*(z)$ at $\bar{V}(z)/\bar{V}_s(z) = 0.125$, and the maximum $\theta_*(z)$ under stable conditions, $\theta_*^{max}(z)$. In (b), (c), and (d) $\alpha(z)$, $\beta(z)$, and $\gamma(z)$ for the MOST bulk formulae under the neutral condition, $\alpha_N^{MOST}(z)$, β_N^{MOST}, and $\gamma_N^{MOST}(z)$, are plotted in black for comparison with the observed neutral values (red in b and c, black circles in d).

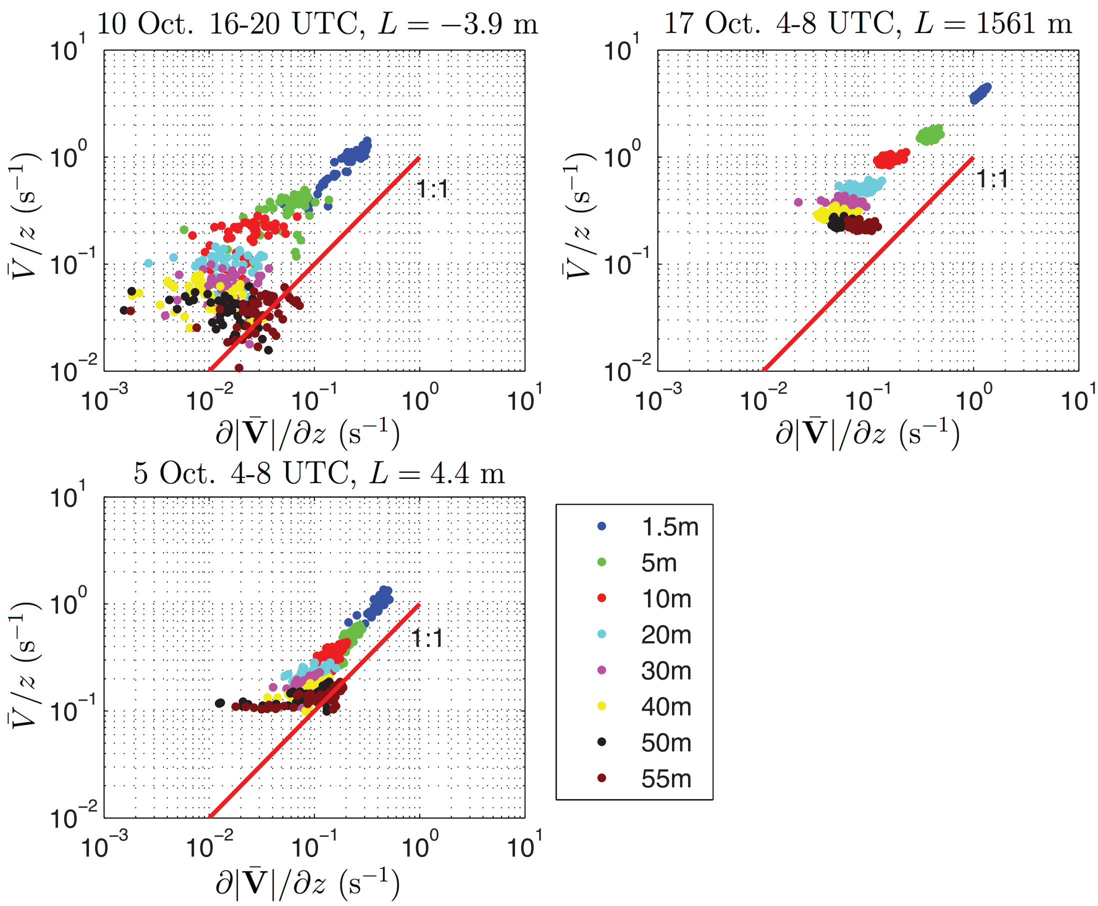

Fig. 14 Relationships between the bulk shear ($\bar{V}(z)/z$) and the local shear ($\partial|\bar{\mathbf{V}}(z)|/\partial z$) at eight observation heights for three different Obukhov lengths, L. Here $\mathbf{V}(\mathbf{z})$ is the wind vector.

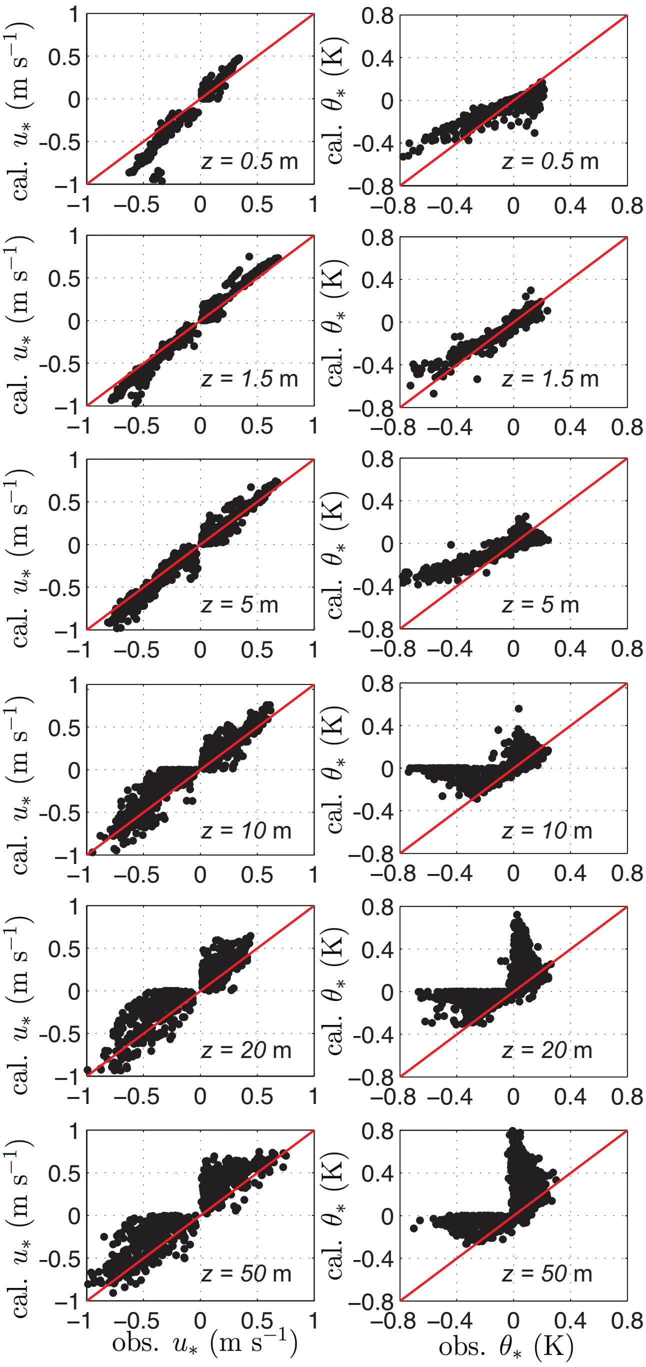

Fig. 15 Comparison between the 30-min observed vs. the calculated daytime and nighttime $u_*(z)$ (left column) and $\theta_*(z)$ (right column) at the selected sonic anemometer heights using the MOST bulk formulae and the stability functions described in Beljaars and Holtslag (1991). The daytime $u_*(z)$ is changed to negative so that the daytime and nighttime $u_*(z)$ can be displayed on one plot. The red lines represent the 1:1 comparison. Here $z_h = 2z_m = 0.1$ m is used in the MOST bulk formula to obtain good agreement with observed $u_*(z)$ below 10 m.